Dynamic Excitation of Internal Gravity Waves in the Equatorial Oceans

B. R. SUTHERLAND

Department of Applied Mathematics and Theoretical Physics, University of Cambridge, Cambridge, United Kingdom

(Manuscript received 31 July 1995, in final form 15 April 1996)

ABSTRACT

It is proposed that shear instability of the upper flank of the equatorial undercurrent may generate, under a broad range of conditions, downward propagating internal gravity waves (IGW) of large amplitude. The generation mechanism is shown to require only that the background stratification is weak where the shear is large (i.e., in the mixing region) and that the stratification is sufficiently large in the far field (i.e., near the thermocline). In a series of studies, the generation of IGW from unstable shear flows is examined. Linear theory is used to predict under what circumstances the generation of IGW may be large, and fully nonlinear simulations restricted to two dimensions are employed to provide estimates of the degree of vertical mixing and of the vertical transport of horizontal momentum by IGW. In particular, the simulations demonstrate that, when large amplitude IGW are generated by shear instability, the mean flow itself is significantly decelerated in the mixing region. The momentum flux associated with the radiating IGW is large, and it is proposed that these may act in part as a momentum source to the deep equatorial countercurrents.

1. Introduction

Well below the surface of the equatorial oceans flow surprisingly strong zonal jets. In the equatorial Pacific Ocean, for example, alternating eastward and westward currents have been observed at depths between 500 and 3000 m, flowing at instantaneous velocities as great as 25 cm s^{-1} (Firing 1987). These currents, referred to hereafter as "zonal countercurrents," are confined to within 2° latitude about the equator. Similar observations have been made in the equatorial Atlantic Ocean (Eriksen 1982) and the equatorial Indian Ocean (Luyten and Swallow 1976). Zonal countercurrents have been observed to persist for very long times and, in particular, Eriksen (1985) observed no significant temporal variations of the large-scale features of the zonal countercurrents over the two years of the PEQUOD experiment of 1981–83. Although an understanding of the structure of the currents has improved in recent years, the sources of energy and momentum that drive the zonal countercurrents have not yet been clearly identified. In several of the forcing mechanisms that have been proposed, the zonal countercurrents are modeled in linear theory by equatorial waves that are generated either at the western boundary by the reflection of Kelvin waves (Clark 1983) or at the eastern boundary (Harvey and Patzert 1976; Longsdale 1977). As pointed out by Muench et al. (1994), however, the time required for the generation and maintenance of equatorial waves by these mechanisms is too great in the presence of dissipative effects. In light of this observation, they proposed that the zonal countercurrents are most likely to be generated by the deposition of momentum and energy in the ocean interior through either internal instabilities or wave–wave interactions. It is reasonable to suppose, therefore, that the zonal countercurrents are driven by disturbances that propagate downward from near the ocean surface where the energy density is large.

Concurrently, many authors have recently proposed that internal gravity waves (hereafter referred to as IGW) may be responsible for transporting horizontal momentum downward from the surface mixed layer of the equatorial oceans, and generating turbulence and drag near the core of the equatorial undercurrent (Dillon et al. 1989; Hebert et al. 1991; Skyllingstad and Denbo 1994). In particular, Wijesekera and Dillon (1991) have proposed a mechanism whereby convective plumes quasiperiodically deform the base of the mixed layer and generate IGW. By way of nonlinear simulations, Skyllingstad and Denbo (1994) have demonstrated a mechanism whereby IGW are generated in the mixed layer by what they identified as Tollmein–Schlichting instability. In both cases the IGW propagate at horizontal phase speeds comparable to the zonal velocity of the upper flank of the equatorial undercurrent. Since, as first pointed out by Bretherton (1969), IGW deposit momentum to the mean flow near a critical level, these mechanisms may act as sources of drag to the equatorial undercurrent, but they do not seem to

Corresponding author address: Dr. Bruce R. Sutherland, Department of Applied Mathematics and Theoretical Physics, University of Cambridge, Silver Street, Cambridge CB3 9EW, United Kingdom.
E-mail: brs21@damtp.cam.ac.uk

represent a likely source for IGW that propagate downward below the equatorial undercurrent and deposit momentum in the deep ocean.

In this paper an alternative mechanism for the generation of IGW is proposed, which may, at least in part, account for both the drag exerted on the equatorial undercurrent and for the source of momentum and energy that drives the zonal countercurrents. It is shown herein that instability of the upper flank of a model equatorial undercurrent situated well below the surface mixed layer may generate IGW, which propagate downward to the deep ocean. Thus, drag may be exerted on the upper flank of the equatorial undercurrent not only by the deposition of momentum by breaking IGW but also by the extraction of momentum by IGW generation as shown schematically in Fig. 1.

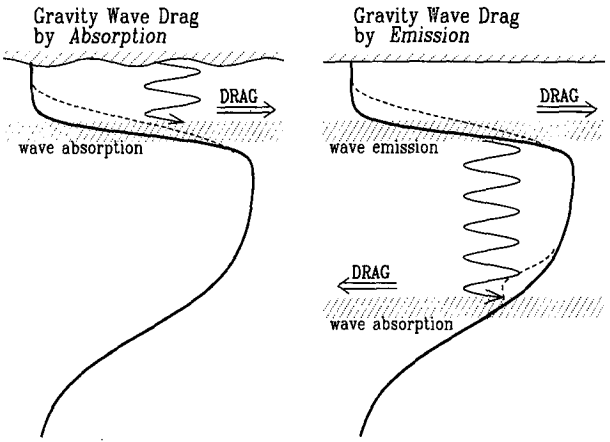

FIG. 1. The schematic represents two mechanisms by which IGW may exert drag in the equatorial undercurrent. The left-hand diagram demonstrates a mechanism for wave drag via absorption of IGW generated in the surface mixed layer. The right-hand diagram demonstrates a mechanism for wave drag via wave emission in a dynamically unstable flow that is shear unstable on the upper flank of the jet. IGW generated by this mechanism propagate downward to great depths where they may be reabsorbed at a critical level, for example, on the lower flank of the equatorial undercurrent. In both diagrams, double horizontal arrows indicate the direction of wave drag, which is significant in the stippled region. The thick solid curve is a profile of the mean flow for a model equatorial undercurrent, and the thin dashed curve illustrates a typical state to which the mean flow may evolve under the decelerating influence of wave drag.

Previous attempts to demonstrate the existence of a coupling between shear instability and IGW radiation have been made by many authors in studies of the atmosphere including early work by Lindzen and Rosenthal (1976), Lalas and Einaudi (1976), and Davis and Peltier (1976), who examined the linear stability of a uniformly stratified shear flow in the presence of a rigid floor. In each study, the growth rate of the normal mode that coupled with radiating IGW was significantly less than the growth rate of the (nonradiating) most unstable normal mode, and so it was unclear whether radiation would in fact occur as the flow developed nonlinearly. The effectiveness of this mechanism was cast into further doubt after McIntyre and Weissman (1978) explained that since the depth of penetration of a normal mode disturbance into a region of large N^2 was inversely proportional to the growth rate of the disturbance, one might expect that the mixing region would become strongly nonlinear before any significant radiating disturbance could develop in the far field. They concluded that a nonlinear assessment would be necessary to ascertain whether a given basic state was capable of radiating IGW. Thereafter, followed attempts to examine whether IGW may be generated by nonlinear mechanisms such as, for example, subharmonic excitation (vortex pairing) (Davis and Peltier 1979) and wave–wave interactions (envelope radiation) (Fritts 1982; Chimonas and Grant 1984a; Chimonas and Grant 1984b). However, neither of these two mechanisms seemed adequate to explain the observed prevalence of large amplitude IGW associated with the tropospheric jet stream (Fritts and Nastrom 1992).

Only recently has an efficient mechanism for large amplitude IGW generation by shear instability been identified. By way of fully nonlinear simulations of Boussinesq flow restricted to two dimensions, Sutherland and Peltier (1994) demonstrated that IGW may be generated in a flow in which the buoyancy frequency N is small in the region of strong shear and is sufficiently large in the far field. They showed that the excitation mechanism is robust and, furthermore, they argued that such a precondition of IGW generation may occur spontaneously in nature under circumstances where mixing in a continuously reinforced shear layer consequently reduces N in the mixing region. In their analysis of the characteristics of the waves in the later stages of the nonlinearly developing flow, they showed that the emitted waves maintained approximately the same phase speed as that of the most unstable normal mode calculated for the initial basic state. Indeed, Sutherland et al. (1994), upon reexamination of the result of McIntyre and Weissman (1978), showed that it is possible to predict on the basis of linear theory whether large amplitude IGW are generated by a dynamically unstable shear flow. In qualitative terms, they proposed that shear-generated IGW would propagate into a region of constant N if the vertical structure of the most unstable normal mode disturbance was sufficiently "wavelike" over the depth of penetration of the disturbance. Specifically, they estimated that large amplitude IGW should radiate if the ratio of the real to imaginary parts of the vertical wavenumber in the far field exceeds unity [e.g., see Eq. (9) and the discussion that follows]. This was referred to by the authors as the "penetration condition."

The result is generic and has been successful in the analysis of idealized jet and shear flows (Sutherland et al. 1994) and of a model tropospheric jet (Sutherland and Peltier 1995) in nonlinear numerical simulations. An intuitive explanation for this assumption is that

large-scale vortices may develop in the mixing region and periodically excite IGW in the surrounding fluid where N is sufficiently large to support a broad frequency spectrum of IGW. This view is too simplistic, and a more satisfactory explanation requires an understanding of the interactions between the radiating IGW and the mixing region. These ideas will be expanded upon herein.

In section 2 vertical profiles of the zonal current and squared buoyancy frequency observed by Hebert et al. (1992) during an overturning event in the mixing region of the equatorial Pacific Ocean are used to motivate a detailed survey of dynamically unstable basic states that may generate IGW. As pointed out by Pedlosky (1987, §7.1), observed mean flow profiles cannot be used as an initial state from which to perform a stability analysis because these inherently average over fluctuations that, in most cases, give a basic state that is more stable than the fluctuation free state. Instead, analytically defined basic-state profiles are examined here. The large-scale features of the observed flow are thus represented by a small number of parameters that may be adjusted to examine the stability and evolution of the flow for a range of initial conditions. Specifically, this study examines in detail the effect of varying two parameters that represent the degree of stratification in the mixing region and in the far field. Linear stability analysis of the initial condition specified by these two parameters is employed to find the most unstable normal mode, the characteristics of which determine whether the generation of large amplitude IGW are anticipated.

In section 3, fully nonlinear numerical simulations of stratified, Boussinesq two-dimensional flow are performed for a range of cases in which the stratification within the mixing region and well below the mixing region is varied. These simulations serve to test whether large amplitude IGW predicted by linear theory do occur and also to provide a crude assessment of the intensity of IGW radiation.

A discussion of the results and their geophysical significance follows in section 4. Therein some speculation is given concerning which physical preconditions may be necessary for the IGW generation mechanism to operate and concerning the propagation of IGW below the undercurrent core in the real ocean.

2. Assessment of IGW generation by linear theory

The supposition motivating this survey of the linear stability of stratified shear flows is that IGW are generated by shear instability provided that N is sufficiently small in the region of strong shear but is sufficiently large in the far field. Because the IGW of interest here have relatively small horizontal extent (i.e., horizontal wavelengths on the order of 100 m), and because their excitation, if it occurs, would be intermittent, there is little direct evidence of IGW coupling with shear instability. However, one observation that lends credible evidence for this mechanism is given by Hebert et al. (1992) who, as part of the Tropic Heat program, have reported detailed observations during the morning of 16 April 1987 at the equator near 135°W of a horizontally confined IGW wavepacket associated with an overturning event extending approximately between 25-m and 55-m depth. The solid curve in Fig. 2a is a representation of the hourly averaged zonal flow across the depth of the unstable region during the time over which the wavepacket was observed. Although the maximum eastward velocity shown is 0.9 m s^{-1} at approximately 65-m depth, the actual core of the equatorial undercurrent as observed between 5 and 15 April was situated on average at approximately 120-m depth, and on 16 April was displaced upward by the presence of an underlying inertia–gravity wave (Peters et al. 1991, 1995). The dashed curve in Fig. 2a is the profile of N^2 determined from the potential density profile observed shortly before the disturbance was observed. The gradient Richardson number $\mathrm{Ri}(z) = N^2/(dU/dz)^2$ gives a measure of the stabilizing effect of the stratification compared with the destabilizing effect of shear. As pointed out by Miles (1961) and Howard (1961), if Ri is greater than $1/4$, a stratified parallel flow is stable to normal mode disturbances and instability may be anticipated where $\mathrm{Ri} < 1/4$. Although the observed flow was not parallel and U and N^2 were not recorded at the same point in the flow, the basic-state profiles give a crude estimate of the flow stability. Figure 2b shows the profile of Ri for the basic states in

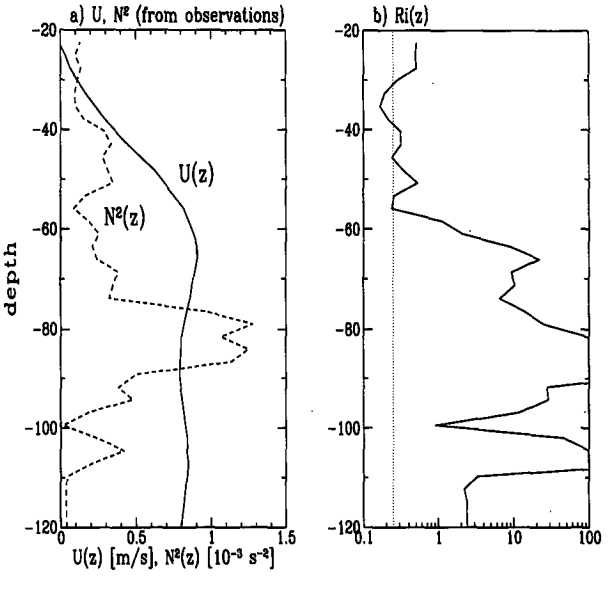

FIG. 2. (a) Profiles of the zonal flow and N^2 based on observations by Hebert et al. (1992). (b) The gradient Richardson number Ri calculated for the basic state in (a). Note the basic state is near marginal stability between -55 m $< z < -30$ m in the sense that Ri ≈ 0.25 over this range.

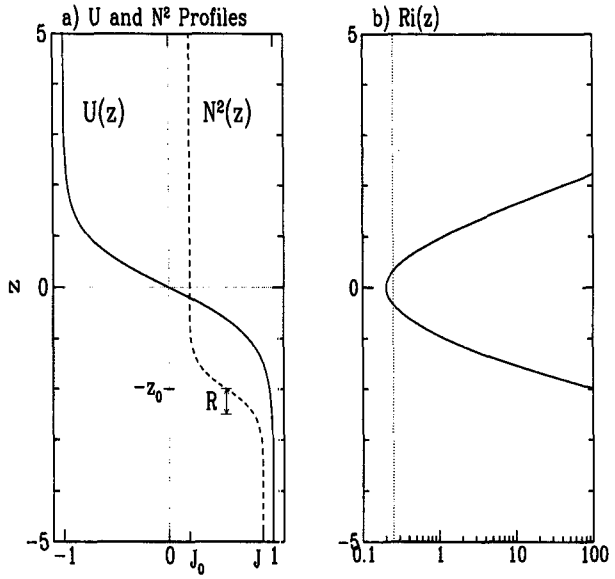

FIG. 3. Typical basic state used for the studies herein based upon an analytic approximation, given by Eq. (2), to the large-scale features shown in Fig. 2: (a) $U(z)$ (solid line) and $JN^2(z)$ (dashed line), shown for parameters $J_0 = 0.2$, $J = 0.9$, $z_0 = 2$, $R = 0.5$; (b) gradient Richardson number corresponding to basic state in (a).

Fig. 2a, the vertical dashed line representing the critical value Ri = 1/4. The diagram shows that the mean flow may be unstable at depths as great as 70 m.

Whether an instability, if it occurs, couples with radiating IGW will be shown to depend sensitively on the large-scale features of the mean flow. The stability and evolution of the observed flow is examined by studying the basic state with analytic profiles of horizontal velocity U_* and squared buoyancy frequency N_*^2, given by

$$\left.\begin{aligned} U_*(z) &= \mathrm{U0}_* - \mathcal{U}\tanh[(z_* + zc_*)/\mathcal{L}] \\ N_*^2(z) &= \mathrm{Ns}_*^2 + \frac{1}{2}(\mathrm{Nt}_*^2 - \mathrm{Ns}_*^2) \\ &\quad \times \{1 - \tanh[(z_* + z0_*)/R_*)]\} \end{aligned}\right\} \quad (1)$$

in which the asterisk subscript is used explicitly to denote dimensional fields. The horizontal velocity profile is characterized by the depth of the maximum shear, $-zc_*$; the horizontal speed of the flow at this depth, $\mathrm{U0}_*$; the difference between the flow speed at this depth and at great depths, $\mathcal{U}$; and the vertical extent over which the flow increases to this speed, $\mathcal{L}$. Here $N_*(z)$ is characterized by the buoyancy frequency near the surface Ns_* and at the thermocline Nt_*, the depth of where N_*^2 increases most quickly, $-z0_*$, and the vertical extent over which N_*^2 increases, R_*. The assumption here is that the small-scale structures of the observed flow do not significantly affect the large-scale stability characteristics. Of course, the equatorial undercurrent has a jet and not a shear structure, and N_*^2 decreases below the thermocline. However, the flow structure at great depths is assumed to have a negligible effect upon the early evolution of the instability in the mixing region, and it is therefore convenient to assume that the velocity and buoyancy frequency at great depths are constant so that the characteristics of IGW generated by shear instability may easily be examined. The hyperbolic tangent shear flow has often been used in studies of the stability of shear flows both for its generic structure and because analytic solutions exist for the curves of marginal stability of this flow in uniformly stratified fluid (Drazin and Howard 1966; Hazel 1972) and in stratified fluid characterized by $N^2 = J0 + J1\tanh^{2n}(z)$ (Lott et al. 1992).

It is convenient to distil from the basic state, Eq. (1), the essential parameters that govern the behavior of the flow evolution. To this end, the basic state is evaluated in nondimensional units with respect to a frame of reference moving at speed $\mathrm{U0}_*$ in a vertical coordinate system with origin at the shear maximum. Taking $\mathcal{U}$ and $\mathcal{L}$ as the characteristic velocity and length scales, respectively, the nondimensional basic state is given by

$$\left.\begin{aligned} U(z) &= -\tanh(z) \\ JN^2(z) &= J_0 + \frac{1}{2}(J - J_0) \\ &\quad \times \{1 - \tanh[(z + z_0)/R)]\} \end{aligned}\right\} \quad (2)$$

in which $z = (z_* + zc_*)/\mathcal{L}$, $z_0 = (z0_* + zc_*)/\mathcal{L}$, $R = R_*/\mathcal{L}$, $U = U_*/\mathcal{U}$, $J = (\mathrm{Nt}_*\mathcal{L}/\mathcal{U})^2$, $J_0 = (\mathrm{Ns}_*\mathcal{L}/\mathcal{U})^2$, and $JN^2 = (N_*\mathcal{L}/\mathcal{U})^2$. The four parameters J, J_0, z_0, and R are nonnegative and allow the analysis of circumstances under which waves may be generated in a stratified fluid where JN^2 increases from J_0 to J over a vertical distance determined by R at a distance z_0 below the maximum shear of the background flow. For example, the basic state for parameters $J = 0.9$, $J_0 = 0.2$, $z_0 = 2$, and $R = 0.5$ is shown in Fig. 3a and the corresponding profile of the gradient Richardson number is shown in Fig. 3b.

A wide variety of observed zonal flows in the mixing region of the equatorial oceans may be modeled in the form of Eq. (2). For reference, Table 1 lists the relevant dimensional and nondimensional parameters estimated from one of the basic states observed by Hebert et al. (1992), which is represented in Fig. 2a. In particular, the characteristic length scale based upon the shear half-depth is $\mathcal{L} \approx 10$ m and the characteristic velocity scale is $\mathcal{U} \approx 0.4$ m s^{-1}. Because the instantaneous basic state immediately preceding the instability may be moderately different from the time-averaged basic state [e.g., see Pedlosky (1987), §7.1], the stability and flow evolution are examined for a range of parameters to examine under what conditions large am-

TABLE 1. Relevant dimensional parameters and wave characteristics estimated from observations by Hebert et al. (1992), and for four stimulations studied here in detail with the basic state prescribed analytically by Eq. (2). The characteristic length and velocity scales based on the shear half-depth are $\mathcal{L} \approx 10$ m and $\mathcal{U} \approx 0.4$ m s^{-1}. Where the shear is strongest the flow speed is taken to be ≈ 0.5 m s^{-1}. For the simulations, the horizontal wavelength λ_x and phase speed c_{px} are determined from the most unstable mode of linear theory. From nonlinear simulations the peak Reynolds stress in time τ_{max} is determined 50 m below the initial level of maximum shear. $\bar{D}$ estimates the average deceleration in the mixing region due to extraction of momentum by IGW generation. It is calculated over the duration of each simulation (about 42 min) assuming the drag due to IGW emission extends uniformly over a 100-m depth in the mixing region.

	Observed flow	$J_0 = 0$		$J_0 = 0.05$	
		$J = 0.4$	$J = 0.2$	$J = 0.4$	$J = 0.2$
Ns_* (10^{-2} s^{-1})	1.5	0	0	0.9	0.9
Nt_* (10^{-2} s^{-1})	3.5	2.5	1.8	2.5	1.8
λ_x (10^2 m)	1.0	1.3	1.3	1.1	1.2
c_{px} (m s^{-1})	0.2	0.5	0.5	0.5	0.5
τ_{max} (N m^{-2})		8.8	5.6	4.5	0.7
$\bar{D}$ (10^{-5} m s^{-2})		2.9	1.0	2.6	0.1

plitude IGW are excited. Four of these cases are discussed in detail below, and the parameters determining the basic state of each are given in dimensional variables in Table 1 using $\mathcal{L} \approx 10$ m and $\mathcal{U} \approx 0.4$ m s^{-1}. For each case, Table 1 also lists the horizontal wavelength and phase speed of the most unstable mode, as well as the average deceleration $\bar{D}$ of the mixing region due to the extraction of momentum by IGW as determined by nonlinear simulations.

In order to assess whether a given basic state is capable of generating IGW by way of shear instability to normal mode disturbances, the characteristics of the most unstable mode must first be determined, and it is not apparent before such a calculation precisely what those characteristics might be. Such considerations are important since, as will be demonstrated, a small change to the basic state may result in small changes to the characteristics of the most unstable mode but large changes in the radiative behavior of IGW. To gain intuitive insight into which unstable basic states are capable of linearly exciting IGW, a survey is presented here of the stability characteristics of a shear flow in a variable N^2 environment.

If the fluid is assumed to be inviscid, the linear stability of a given basic state to the growth of normal modes may be determined by solving the (nondimensional) Taylor–Goldstein equation

$$\phi''(z) + \gamma(z)^2\phi(z) = 0, \tag{3}$$

in which

$$\gamma = \sqrt{\frac{JN^2(z)}{(U(z) - c)^2} - \frac{U''(z)}{U(z) - c} - \alpha^2}. \tag{4}$$

Here $\phi(z)$ is the perturbation streamfunction amplitude and c is the (complex) phase speed of the mode with horizontal wavenumber α. The square root on the right-hand side of Eq. (4) may be complex and, without loss of generality, the branching condition

$$0 < \arg(\gamma) \leq \pi \tag{5}$$

is required so that, in light of the form of Eq. (3), $+\gamma$ may be interpreted as the complex vertical wavenumber of an upward propagating disturbance and $-\gamma$ may be interpreted as the complex vertical wavenumber of a downward propagating disturbance. Indeed, where N^2 and $U = U_{-\infty}$ are constant and if c is real, Eq. (4) is just the dispersion relation for IGW of intrinsic frequency $\Omega = \alpha(c - U_{-\infty})$.

A shooting code is used to integrate Eq. (3) for a range of α as described in Sutherland and Peltier (1992). In this method the streamfunction is found for a particular value of α by first estimating the phase speed c and then integrating from where $JN^2 \approx J_0$ to where $JN^2 \approx J$. The integration starts and ends at vertical positions sufficiently far from the mixing region where the amplitude of the streamfunction at the boundaries is negligibly small. The top and bottom boundary conditions are set to allow radiating solutions. However, the amplitude of the normal mode is found to be sufficiently small near the boundaries that the stability calculation performed for a domain with rigid boundaries gives similar results. After integrating using an initially estimated (complex) value of $c = c_r + ic_i$, the phase speed is then systematically adjusted until c converges to an eigenvalue for which the corresponding eigenfunction satisfies the lower boundary conditions. The solution of Eq. (3) for the particular α for which the growth rate $\sigma = \alpha c_i$ is greatest is identified with the streamfunction amplitude of the most unstable mode.

First, a case is examined in which N^2 increases from J_0 to J over a small vertical range and at a moderately far distance from the mixing region. In particular, for the case with $z_0 = 3$, $R = 0.1$, the phase speed and growth rate for specific values of J_0 and J are calculated over a range of horizontal wavenumbers α as shown in Fig. 4. The growth rates as a function of the horizontal wavenumber shown in Fig. 4a are calculated for $J_0 = 0.05$ and $J = 0.05$ (solid line), $J = 0.25$ (short-dashed line), $J = 0.50$ (long-dashed line), $J = 0.75$ (short dash–dot), and $J = 1$ (long dash–dot). In Fig. 4b the growth rates are shown for $J = 0.50$ and $J_0 = 0.0$ (solid line), $J_0 = 0.05$ (short-dashed line), $J_0 = 0.10$ (long-dashed line), and $J_0 = 0.15$ (short dash–dot). In every case, the growth rate has a well-defined maximum for some horizontal wavenumber $\alpha = \alpha_c$, which is identified as the wavenumber corresponding to the most unstable mode. The effect of increasing J and keeping J_0 fixed is to decrease moderately the growth rate of the most unstable mode with little effect on α_c. The effect of increasing J_0 and keeping J fixed

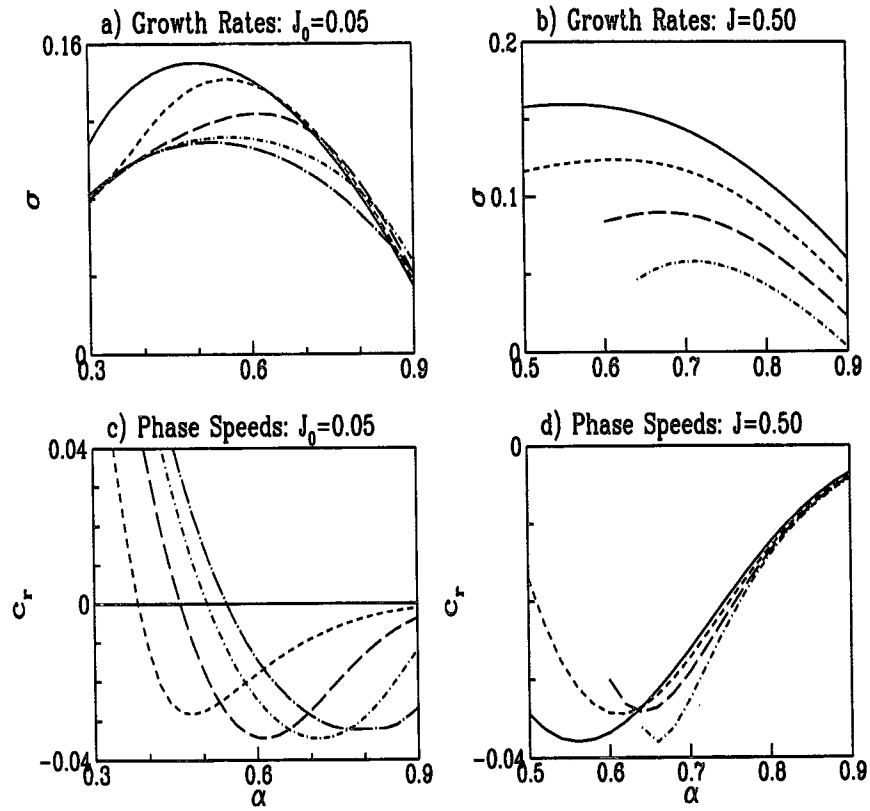

FIG. 4. Properties of unstable normal modes as a function of wavenumber α calculated for a range of basic states with JN^2 given by Eq. (2) with $z_0 = 3$, $R = 0.1$. In (a) and (c) growth rates and phase speeds, respectively, are given for $J_0 = 0.05$ and $J = 0.05$ (solid line), $J = 0.25$, (short-dashed line), $J = 0.50$ (long-dashed line), $J = 0.75$ (short dash–dot), and $J = 1.0$ (long dash–dot). In (b) and (d) growth rates and phase speeds, respectively, are given for $J = 0.50$ and $J_0 = 0$ (solid line), $J_0 = 0.05$ (short-dashed line), $J_0 = 0.10$ (long-dashed line), and $J_0 = 0.15$ (short dash–dot).

is to decrease greatly the growth rate and increase the value of α_c. Figures 4c and 4d show the horizontal phase speeds of the normal modes corresponding to the cases for which the growth rates are shown in Figs. 4a and 4b, respectively. In every case, the horizontal phase speeds are small in comparison with the speed of the background flow at great depths.

Although the flow is unstable over a great range of parameters J_0 and J, the most unstable mode is capable of exciting IGW over only a limited range of parameters. The flux Richardson number, defined by $R_f = -g\langle w'\rho'\rangle/\langle u'w'\rangle(dU/dz)$, is often used to provide a measure of the degree of mixing. It has limited use in the context of this problem, however, because the N^2 and U are uniform at great depths and because the perturbation kinetic energy varies greatly as the unstable flows evolve nonlinearly so that the interpretation of R_f can be ambiguous. A direct measure of the excitation of IGW in an unstable flow is given by comparing the linear correlation coefficient of the horizontal and vertical velocity,

$$\mathrm{corr}(u', w') = \langle u'w'\rangle/\sqrt{\langle u'^2\rangle\langle w'^2\rangle}, \qquad (6)$$

with that of the vertical velocity and perturbation density,

$$\mathrm{corr}(w', \rho') = \langle w'\rho'\rangle/\sqrt{\langle w'^2\rangle\langle \rho'^2\rangle}, \qquad (7)$$

determined from the most unstable mode. For plane small amplitude IGW, $\mathrm{corr}(u', w')$ (which is related to the Reynolds stress) is exactly 1 in absolute value and $\mathrm{corr}(w', \rho')$ (which is related to the vertical density flux) is exactly 0. In general, these correlations provide insight into the degree of momentum transport and mixing by a mode of instability. Figure 5 compares the correlations as a function of depth calculated from the most unstable mode for four cases with $z_0 = 3.0$, $R = 0.1$, and (a) $J_0 = 0$, $J = 0.4$, (b) $J_0 = 0$, $J = 0.2$, (c) $J_0 = 0.05$, $J = 0.4$, and (d) $J_0 = 0.05$, $J = 0.2$. In all four cases the correlations are nonnegative indicating the tendency of the most unstable mode to transport

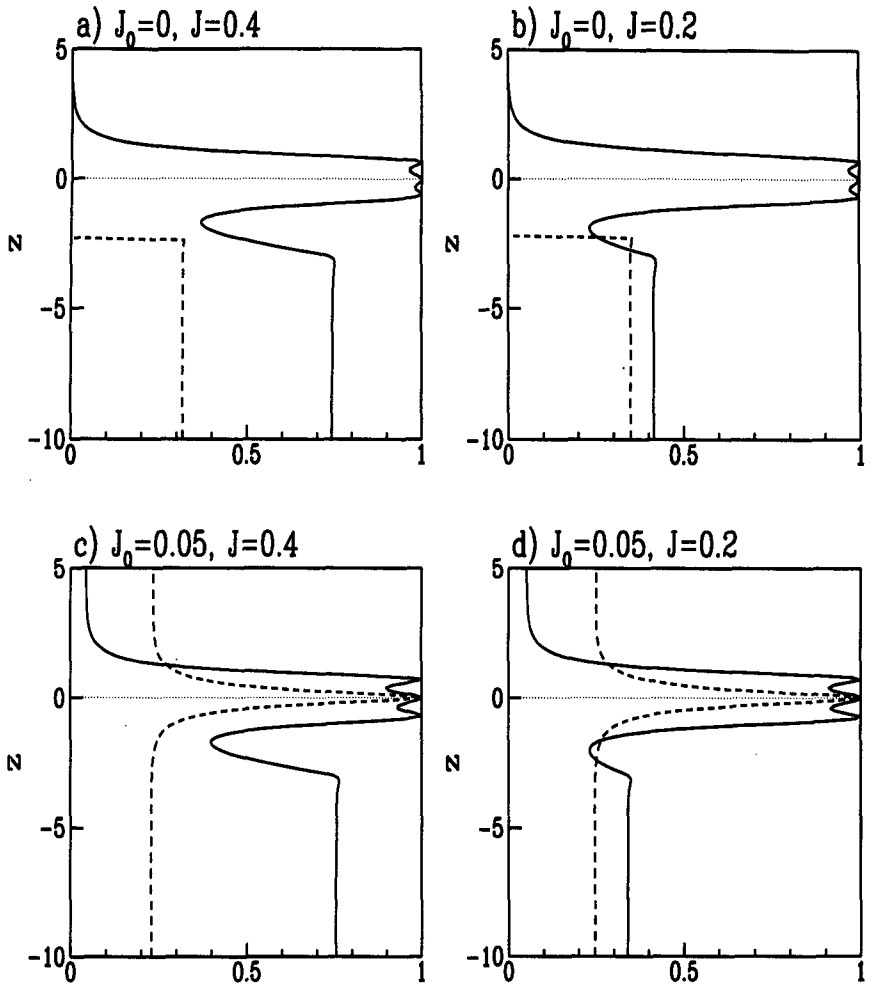

FIG. 5. Profiles of the linear correlation coefficients of horizontal and vertical velocity corr(u', w') (solid line) and of vertical velocity and fluctuation density corr(w', ρ') (dashed line) calculated for the most unstable normal mode of shear flow with JN^2 given by Eq. (2) with $z_0 = 3.0$, $R = 0.1$, and (a) $J_0 = 0$, $J = 0.4$, (b) $J_0 = 0$, $J = 0.2$, (c) $J_0 = 0.05$, $J = 0.4$, and (d) $J_0 = 0.05$, $J = 0.2$.

upstream momentum downward and to displace lighter fluid downward below the mixing region. In all four cases, u' and w' are strongly correlated in the mixing region near $z = 0$. This correlation remains large at great depths in cases (a) and (c), when $J = 0.4$ and the stratification is sufficiently large to support IGW excited directly by the instability. When the mixing region is stratified, w' and ρ' are strongly correlated near $z = 0$ but become more decorrelated at great depths. In fact, corr(w', ρ') is smaller at great depths when the mixing region is more strongly stratified. The diagrams demonstrate the significant transition in the mixing properties of an unstable flow that occurs when stratification at great depths becomes sufficiently large: the transport of momentum by waves is strongly enhanced whereas the transport of mass by waves is relatively unchanged.

These observations invite the question, for which values of J_0 and J is IGW radiation expected to occur? As pointed out by Lindzen (1974) and McIntyre and Weissman (1978), among others, the direct excitation of IGW by an unstable normal mode should not occur if the intrinsic frequency of the mode exceeds the buoyancy frequency in the far field since disturbances of this frequency are evanescent. Thus, a necessary condition for the shear generation of IGW that propagate with horizontal phase speed c_{px} in the far field (in particular, at great depths) where the background flow speed is $U_{-\infty}$ and $JN^2 = J$ is

$$|\Omega| = |\alpha(c_{px} - U_{-\infty})| < \sqrt{J}. \qquad (8)$$

This is known as the "phase speed condition." Recently, Sutherland et al. (1994) proposed a sufficient

condition for IGW excitation by considering the structure of the most unstable mode in the far field, the amplitude of which may decay rapidly with depth if the growth rate of the mode is large. They claimed that an unstable mode, whose structure far from the mixing region has small vertical wavelength compared with the depth of penetration, may continually generate IGW even as the flow becomes strongly nonlinear. They hypothesise that during the growth and nonlinear development of such modes the periodic undulations in the far field may act back upon the mean flow modifying it so that the mixing region continually excites IGW. Explicitly, the sufficient condition (also called penetration condition) states that IGW generation should occur if the absolute value of the ratio $\mathcal{D}$ of the real to imaginary parts of the vertical wavenumber of the most unstable mode in the far field exceeds one. That is,

$$|\mathcal{D}| = |\gamma_r/\gamma_i| > 1. \tag{9}$$

Physically, $\mathcal{D}$ is a measure of the number of vertical wavelengths spanning an e-folding depth of the normal mode in the far field. The critical value 1 is not, strictly speaking, a lower bound but a numerical estimate of the far-field structure of a normal mode that by hypothesis is "sufficiently wavelike." Taking the real and imaginary parts of Eq. (4), the penetration ratio may be expressed in terms of the frequency and growth rate of the normal modes of linear theory. Explicitly, $\mathcal{D}$ is the solution of the quadratic

$$\mathcal{D}^2 - 2\mathcal{B}\mathcal{D} - 1 = 0, \tag{10}$$

in which

$$B = \frac{1}{2}\frac{1}{\Omega\sigma}\left(\frac{1}{J}(\Omega^2 + \sigma^2)^2 - \Omega^2 + \sigma^2\right). \tag{11}$$

Of the two roots of Eq. (10), $\mathcal{D}$ is taken to be that corresponding to energy propagation away from the mixing region. It is a simple matter to show that the phase speed condition and the penetration condition are equivalent in the limit of zero growth rate. It can also be shown, in general, that the penetration condition is satisfied only if the phase speed condition is satisfied.

The range of parameters for which either of these conditions is satisfied is illustrated in Fig. 6, which plots the critical value J^c against J_0 for which the most unstable mode calculated for $R = 0.1$ satisfies (a) $|\mathcal{D}| = 1$ and (b) $\Omega = \sqrt{J}$. In both diagrams, J^c as a function of J_0 is shown for $z_0 = 3.0$ (solid curve), 2.6 (small dash), 2.2 (long dash), 1.8 (small dash–dot), and 1.4 (long dash–dot). Note that for $J_0 \geqslant 0.25$ the flow is stable. For both the phase speed and the penetration conditions, stronger stratification (large J^c) is necessary in the far field for IGW generation when the vertical level (z_0) where JN^2 increases is closer to the region of strong shear. For fixed z_0, J^c determined for the phase speed condition is smallest for $J_0 = 0$ and is as small as ≈ 0.25 for $z_0 = 3$. For small values of J_0, J^c determined for the penetration condition is predicted to be moderately larger than that predicted for the phase speed condition, although J^c for both conditions is comparable if $J_0 > 0.1$. The region of parameter space where the phase speed condition is satisfied but the penetration condition is not satisfied provides a convenient location in which to investigate the effectiveness of the two conditions in characterizing the efficiency of IGW excitation by unstable normal mode development. These predictions are compared with the results of nonlinear simulations discussed in the following section.

3. Nonlinear simulations

The linear stability analysis in section 2 demonstrates that the IGW generation process is robust in the sense that waves are predicted to be excited by the most unstable mode for a broad class of basic states. The manner in which IGW are excited as the normal mode grows in amplitude and breaks in the mixing region is examined by way of fully nonlinear analyses.

The nonlinear simulations are performed by numerically solving the primitive equations for incompressible, Boussinesq flow that is restricted to two spatial dimensions. These are represented numerically in a model based on the methodology developed by Smyth and Peltier (1989) for the study of the evolution of Kelvin–Helmholtz and Holmboe waves. The fully nonlinear equations for momentum conservation and for the conservation of internal energy are, respectively,

$$\frac{Du_*}{Dt_*} = -\frac{1}{\rho_0}\frac{\partial p'_*}{\partial x_*} + \nu\nabla_*^2 u_*, \tag{12}$$

$$\frac{Dw_*}{Dt_*} = -\frac{1}{\rho_0}\frac{\partial p'_*}{\partial z_*} - g\rho'_* + \nu\nabla_*^2 w_*, \tag{13}$$

and

$$\frac{D\rho'_*}{Dt_*} = N_*^2 w_* + \kappa\nabla_*^2\rho'_*, \tag{14}$$

in which the dimensional fields are of horizontal velocity u_*, vertical velocity w_*, fluctuation density ρ'_*, and fluctuation pressure p'_*. The fluctuation pressure p'_* is the total pressure minus the pressure $\bar{p}_*(z)$ that is in hydrostatic balance with the background density $\bar{\rho}_*(z)$. Here $D/Dt_* = \partial/\partial t_* + u_*\partial/\partial x_* + w_*\partial/\partial z_*$ is the material derivative.

As with the linear theory in section 2, Eqs. (12), (13), and (14) are reexpressed in nondimensional form by the substitutions $(x_*, z_*) \rightarrow \mathcal{L}(x, z)$, $t_* \rightarrow (\mathcal{L}/\mathcal{U})t$, $(u_*, w_*) \rightarrow \mathcal{U}(u, w)$, $\rho'_* \rightarrow (\rho_0\mathcal{L}/\mathcal{H})\rho'$, $\overline{\rho_*} \rightarrow (\rho_0\mathcal{L}/\mathcal{H})\bar{\rho}$, and $p'_* \rightarrow \rho_0\mathcal{U}^2 p'$, in which $\mathcal{H}$ is the length scale of background density variations with height. For the validity of the Boussinesq approximation, $\mathcal{H} \gg \mathcal{L}$. With these substitutions, the nondimensional form of the equations are

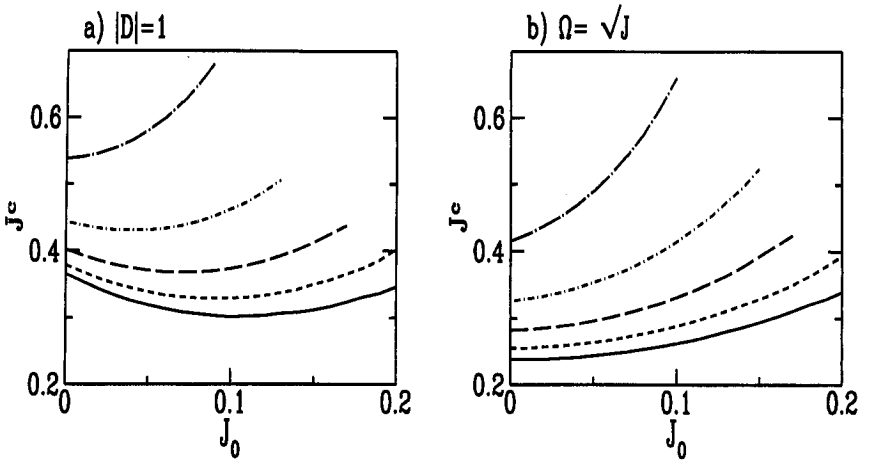

FIG. 6. Values of J_0 and J in Eq. (2) for which the most unstable mode of linear theory satisfies (a) the penetration ratio $|\mathcal{D}| = 1$ and (b) the critical phase speed condition for which the Doppler shifted frequency equals the Brunt–Väisälä frequency in the far field. In both diagrams $R = 0.1$ and $z_0 = 3.0$ (solid line), 2.6 (short-dashed line), 2.2 (long-dashed line), 1.8 (short dash–dot), 1.4 (long dash–dot).

$$\frac{Du}{Dt} = -p'_x + \frac{1}{\mathrm{Re}}\nabla^2 u \tag{15}$$

$$\frac{Dw}{Dt} = -p'_z - J\rho' + \frac{1}{\mathrm{Re}}\nabla^2 w \tag{16}$$

and

$$\frac{D\rho'}{Dt} = N^2 w + \frac{1}{\mathrm{Re\ Pr}}\nabla^2\rho'. \tag{17}$$

The nondimensional parameters of the model are the Reynolds number $\mathrm{Re} = \mathcal{U}\mathcal{L}/\nu$ in which ν is the kinematic viscosity, the Prandtl number $\mathrm{Pr} = \nu/\kappa$ in which κ is the thermal diffusivity, and the bulk Richardson number $J = (g/\mathcal{H})(\mathcal{L}/\mathcal{U})^2$ in which g is the acceleration of gravity.

In practice, Eq. (15)–(17) are solved in the vorticity–streamfunction form since the model then reduces to the evolution equations for only two coupled fields, namely, the vorticity ω and the density fluctuation ρ'. Taking the curl of Eqs. (15) and (16) gives the vorticity equation

$$\frac{D\omega}{Dt} = J\rho'_x + \frac{1}{\mathrm{Re}}\nabla^2\omega, \tag{18}$$

in which $\omega = u_z - w_x$ is the spanwise component of vorticity. The streamfunction is found by inverting the elliptic differential equation

$$\nabla^2\psi = -\omega, \tag{19}$$

and from ψ the components of the velocity vector $\mathbf{u} = (u, w)$ may be determined from $u = -\partial\psi/\partial z$, $w = \partial\psi/\partial x$.

Of Eqs. (17) and (18), the only solutions considered are those that are periodic in the streamwise (horizontal) direction having wavenumbers that are integral multiples of the wavenumber of the most unstable mode $\alpha = 2\pi/\lambda$, in which λ is the horizontal wavelength of the most unstable mode. The length of the channel is set to be $L_x = \lambda$. Accordingly, the horizontal structure of the dependent fields may be represented in a Fourier basis via

$$f(x, z, t) = \sum_{m=-M}^{M} f_m(z, t)\exp(\iota\, m\alpha x) \tag{20}$$

in which f may represent ω or ρ, and M determines the limit of horizontal resolution of each field. The vertical structure of the dependent variables is represented in finite difference form so that ω and ρ are sampled at $P + 1$ equally spaced points $z_0, \ldots, z_P$, spanning the channel of vertical extent L_z, and vertical derivatives are replaced by their second-order finite-difference equivalent. The resulting set of evolution equations is stepped forward in time using a leapfrog method with an Euler backstep taken at regular time intervals to minimize splitting errors. Typically, simulations are terminated at time $t = 100$, before waves grow to large amplitude near the lower boundary of the channel. (In dimensional units this is about 42 min based upon $\mathcal{L} = 10$ m and $\mathcal{U} = 0.4$ m s^{-1}.) To ensure that the results of the simulations are not sensitive to the resolution, simulations are performed for channels of varying width and the equations are integrated with varying spatial resolution, always ensuring that the time step is sufficiently small for numerical stability. The vertical grid spacing is taken to be $dz \approx 0.1$ and, depending on the value of the horizontal wavelength of the most un-

stable mode, the equivalent horizontal grid spacing is $dx \approx 0.1$.

In this mixed spectral–finite difference scheme, modal budgets of quadratic quantities that are conserved in the absence of viscous and thermal diffusion may be assessed by means similar to those employed by Smyth and Peltier (1992). As the simulated fields evolve, they are analyzed to ensure that the rate of energy loss is balanced by diffusion to machine precision. This and the additional diagnostic analyses employed to understand the basic physical interactions governing the flow dynamics are described in further detail in the subsections below.

The vertical profiles of horizontal velocity and JN^2 are taken to be initially of the form given by Eq. (2). The linear stability of basic states in this form has previously been discussed in section 2.

In order to initialize the nonlinear simulations, the background fields of density and horizontal velocity are perturbed by addition onto the basic state of a small amplitude random component as well as a fluctuation having the spatial structure of the fastest growing mode of linear theory determined on the basis of a Galerkin stability analysis employing finite Re and Pr [e.g., Klaassen and Peltier (1985)]. The amplitude of the mode is prescribed such that the maximum vertical velocity in the perturbed flow is initially a small fraction of the characteristic speed. Before accepting numerical results concerning computed disturbance life cycles, it is ensured that the simulations adequately reproduce the exponential growth rate predicted by linear theory. This is done by comparing the linear growth rate to the initial perturbation growth rate σ determined from the simulation by calculating

$$\sigma = \frac{1}{2E'}\frac{dE'}{dt}$$

from the evolving wave kinetic energy E'.

Numerical simulations are performed with Prandtl number Pr = 10 and with moderately large Reynolds number Re = 200. Simulations have also been performed with the same Prandtl number and Re = 400, and with Re = 2000 and Pr = 1. In all cases the large-scale features of the flow and, in particular, the characteristics of radiating IGW are not affected significantly. In the real ocean, the Reynolds number is many orders of magnitude larger. However, it is found in these simulations that the dissipation of energy does not change greatly for Reynolds numbers larger than 2000 because diffusion is enhanced by eddy mixing. Nonetheless, it is because the Reynolds number is unrealistically small that the most unstable mode is explicitly introduced initially. The background flow would otherwise diffuse on an unphysically fast timescale compared with the time for the unstable mode to develop spontaneously from white noise. For the moderately high value of Re that is considered here, the horizontal wavenumber, frequency, and growth rate of the most unstable mode determined by this analysis is found to differ by less than 5% from the corresponding quantities determined by direct integration of the inviscid linear stability equations (3) and (4).

a. Simulations with an unstratified mixing region

To illustrate the range of behavior of the mechanism by which IGW are generated by shear unstable flow, two examples are considered below in which the stratification of the fluid is negligibly small where the shear is large. In the first of these the stratification is sufficiently large in the far field that IGW are excited directly by the growth and nonlinear development of the most unstable mode. In the second example, the stratification in the far field is weaker and a small amplitude IGW wavepacket is generated below the mixing region by a nonlinear mechanism.

The nonlinear evolution of the flow is quite different for cases in which the stratification in the mixing region is nonnegligible. These cases will be examined in section 3b.

First, the evolution is considered of the unstable basic state given by Eq. (2) with parameters $R = 0.1$, $z_0 = 3.0$, $J_0 = 0$, and $J = 0.4$. The results of linear theory have been discussed for this case in section 2, and the characteristics of the most unstable mode are given in Table 2. In particular, the horizontal wavenumber $\alpha \approx 0.50$ and the phase speed $c_{px} \approx -0.014$. (For reference to the real ocean, the dimensional horizontal wavelength and phase speed are estimated in the third column of Table 1 for this case: $\lambda_x \approx 1.3 \times 10^2$ m and $c_{px} \approx 0.5$ m s^{-1}). Therefore, for large negative values of z, the absolute value of the intrinsic frequency $|\alpha(c_{px} - U_{-\infty})| < \sqrt{J}$, so the phase speed condition is satisfied. From the intrinsic frequency and growth rate, $\sigma \approx 0.18$, the penetration ratio may be calculated according to Eqs. (10) and (11), and it is found that

TABLE 2. Characteristics of the most unstable mode of linear theory calculated for four different basic states determined analytically by Eq. (2) with $z_0 = 3$, $R = 0.1$: α is the horizontal wavenumber, c_{px} is the horizontal phase speed, and σ is the growth rate. Also given are the absolute values of the ratio of the intrinsic frequency of the mode to the buoyancy frequency in the far field and of the penetration ratio, which is a measure of the number of vertical wavelengths of the mode over its penetration depth in the far field. The former is used to evaluate the phase speed condition and the latter to evaluate the penetration condition.

Most unstable mode characteristics	$J_0 = 0$		$J_0 = 0.05$	
	$J = 0.4$	$J = 0.2$	$J = 0.4$	$J = 0.2$
α	0.50	0.48	0.55	0.52
c_{px}	−0.014	−0.012	−0.011	−0.008
σ	0.178	0.185	0.141	0.148
$\lvert\alpha(c_{px} - U_{-\infty})/\sqrt{J}\rvert$	0.79	1.08	0.87	1.17
$\lvert\mathcal{P}\rvert$	1.11	0.46	1.15	0.36

$|\mathcal{D}| \approx 1.1 > 1$. Hence, the penetration condition is also satisfied. On the basis of both criteria, the generation of large amplitude IGW is anticipated.

Figure 7 shows the state to which the flow has evolved at time $t = 100$ of the simulation. In (a), contours of vorticity are shown by intervals of 0.1 over a vertical range extending from $z = -10$ to 10. These clearly show the development of a well-defined vortex coupling with IGW that, as can be seen from the upstream phase tilt of the waves, are downward radiating. The vortex structure is qualitatively similar to that studied by many authors [e.g., Zabusky and Deem (1971) and Smyth and Peltier (1989), among others] in the examination of Kelvin–Helmholtz instability. Here, however, although the maximum shear is initially at depth $z = 0$, the vortex center is displaced above this level. In Fig. 7b, the horizontally averaged mean flow at time $t = 100$ (solid line) is compared with the profile of the mean flow at $t = 0$ (dashed line). The inset plots of difference between these flow speeds below the mixing region. This diagram illustrates the significant degree to which the flow is accelerated above $z = 0$ and decelerated below the mixing region due to the downward transport of horizontal momentum by IGW. At time $t = 100$ the shear is largest at $z \approx 1.4$, and this corresponds approximately with the position of the vortex center. The displacement of the vortex core occurs, therefore, because IGW extract horizontal momentum from the mean flow. The deposition of momentum to the mean flow by IGW can likewise be significant. As the inset diagram shows, IGW decelerate the flow by as much as 0.1 from its initial speed 1.0 at a depth $z \approx -33$, well below the mixing region.

The full extent of the waves is illustrated in Fig. 7c, which shows contours of fluctuation density by intervals of 0.4 over a vertical range from $z = -60$ to 10. The vertical flux of horizontal momentum is given by the (nondimensional) Reynolds stress, $\tau = \langle u'w' \rangle$, and this is shown in Fig. 7d for $z = -60$ to 10. The Reynolds stress is largest at the leading edge of the wavepacket where the amplitude of the IGW is largest. The sign of the Reynolds stress is positive indicating the downward transport of upstream momentum.

These results may be compared with those of a simulation in which IGW are not excited directly by the development of the most unstable mode. In particular, a simulation is examined in which the basic state is given by Eq. (2) with parameters $R = 0.1$, $z_0 = 3.0$, $J_0 = 0$, and $J = 0.2$. Although the horizontal wavenumber, phase speed, and growth rate of the most unstable mode listed in Table 2 for this case are similar to those in the previous case, neither the phase speed condition nor the penetration condition are satisfied; therefore, large amplitude IGW are not expected to be excited directly by the growth of the most unstable mode. Figure 8 shows the state to which this simulation has evolved at time $t = 100$. The vorticity contours given by intervals of 0.1 in Fig. 8a show a well-defined vortex core that couples only weakly with radiating IGW at this time: although the vorticity field is perturbed below the vortex, there is no overall upstream phase tilt apparent between $z = -10$ and $z = 0$ and, therefore, the disturbance in this region is not composed of downward propagating IGW. By comparison with the previous case, more of the momentum associated with the flow accelerated above $z = 0$ is accounted for in the flow decelerated below but near $z = 0$; less momentum is transported away from the mixing region, and the center of the vortex core is displaced only marginally above $z = 0$. The momentum redistribution by mixing and IGW is illustrated explicitly in Fig. 8b, which shows profiles of the initial mean flow (dashed curve) and of the mean flow at time $t = 100$ (solid curve). The peak deceleration of the mean flow at $t = 100$, shown in the inset, is 0.03 occurring near $z = -23$. The deceleration occurs due to the passage of a compact IGW wavepacket generated during the initial stages of the flow evolution. Although the intrinsic frequency of the most unstable mode is too great for IGW to be directly excited in the far field, the wavepacket is believed to be generated due to a nonlinear mechanism, primarily from transient forcing of the far field during the initial development of the vortex in the mixing region. Figure 8c shows contours of fluctuation density by intervals of 0.3 over a vertical range from $z = -40$ to 10 (the full computational domain extends down to $z = -60$). As in Fig. 8a, disturbances have no upstream phase tilt except below $z \approx -15$ where the compact IGW wavepacket is situated. The amplitude of the IGW at the leading edge of the wavepacket is much smaller than is the previous case and it propagates downward at a slower speed, an observation consistent with the fact that the phase tilt of the leading edge of the wavepacket is more vertical. The Reynolds stress profile shown in Fig. 8d over the range $z = -40$ to 10 is positive only where the phase tilt of the waves is upstream, and the peak positive value is less than 20% smaller than that in the previous case.

Therefore, even though IGW may be generated by a nonlinear mechanism when the most unstable mode does not directly excite IGW, these waves are much less effective at transporting horizontal momentum downward and away from the mixing region. This observation is quantified in what follows.

IGW are generated when energy is extracted from the initial mean flow by waves. The equation for the time rate of change of mean kinetic energy is given by taking u times Eq. (15) and w times Eq. (16) together with the incompressibility condition and averaging over the domain to give

$$\frac{\partial \langle \mathrm{KE} \rangle}{\partial t} = -J\langle w\rho' \rangle + \frac{1}{\mathrm{Re}} \langle u\nabla^2 u + w\nabla^2 w \rangle, \quad (21)$$

in which $\mathrm{KE} = (u^2 + w^2)/2$, and the domain averaging operator is defined so that

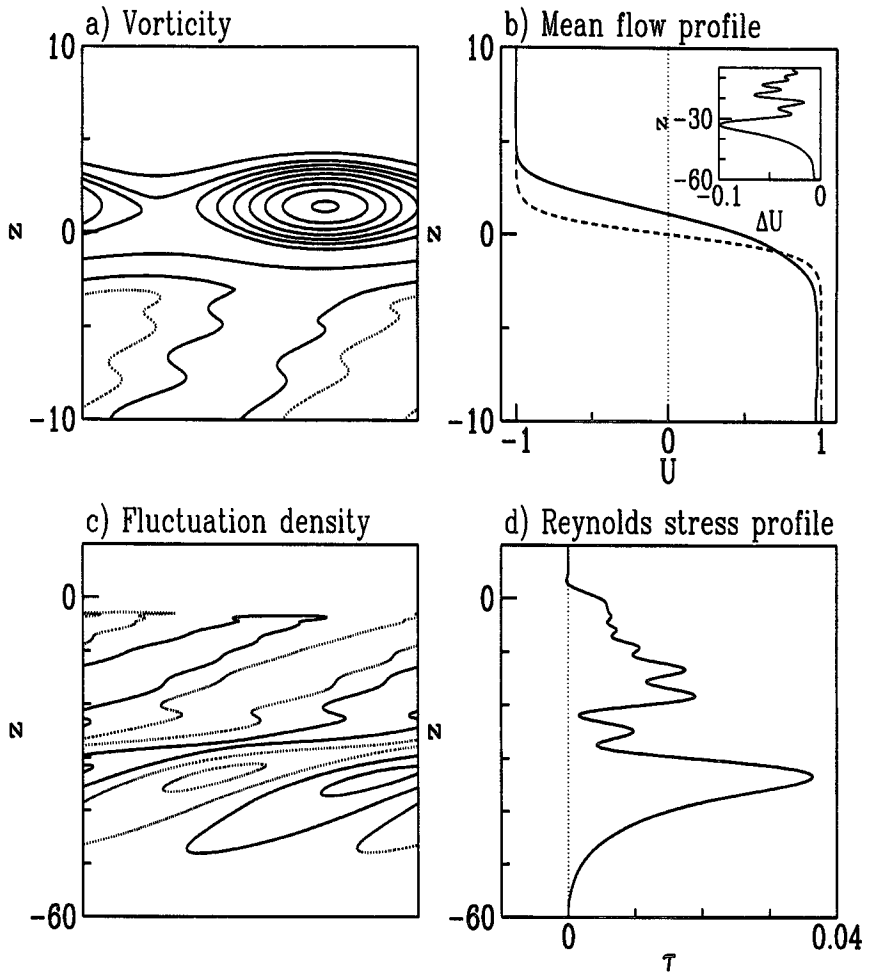

FIG. 7. Development of simulated hyperbolic tangent shear flow for JN^2 characterized by Eq. (2) with $J_0 = 0$, $J = 0.4$, $z_0 = 3$, and $R = 0.1$ at time $t = 100$. (a) Vorticity field shown by contours of 0.1; (b) horizontally averaged mean flow at $t = 100$ (solid curve) compared with mean flow at $t = 0$ (dashed curve), and inset diagram showing difference between these below $z = -5$; (c) fluctuation density field shown by contours of 0.4; and (d) Reynolds stress profile indicating downward transport of upstream momentum.

$$\langle f(x, z)\rangle = \frac{1}{L_x}\int_0^{L_x} dx \int dz f(x, z). \qquad (22)$$

Equation (21) expresses the fact that changes of the domain-averaged kinetic energy occur either due to dissipation or due to the baroclinic conversion of kinetic energy into available potential energy. In order to examine the way in which kinetic energy is extracted from the mean flow by radiating waves, Eq. (21) is further decomposed into terms expressing the change of the mean flow kinetic energy, MKE = $\bar{u}^2/2$, and eddy kinetic energy, EKE = $[(u - \bar{u})^2 + w^2]/2$, in which $\bar{u}(z) = [\int_0^{L_x} u(x, z)dx]/L_x$.

In Fig. 9 the nondiffusive rate of change of mean flow kinetic energy (solid line), the nondiffusive rate of change of eddy kinetic energy (short-dashed line), and the baroclinic conversion of eddy kinetic energy to available potential energy (long-dashed line) are compared between times $t = 0$ and 100 in three simulations. In each case the stratification of the fluid is negligibly small where the shear is large. Here JN^2 is given by Eq. (2) with $R = 0.1$, $z_0 = 3.0$, $J_0 = 0$; and in (a) $J = 0.4$ for which the phase speed and penetration condition are satisfied, in (b) $J = 0.3$ for which only the phase speed condition is satisfied, and in (c) $J = 0.2$ for which neither condition is satisfied. Qualitatively, the simulations are similar up to $t \approx 30$ during which time kinetic energy is extracted from the mean flow by eddies. At $t \approx 11$ in all three cases, the amplitude of the most unstable mode begins to saturate and a vortex develops. Although some eddy kinetic energy is returned to the mean flow during the development of the

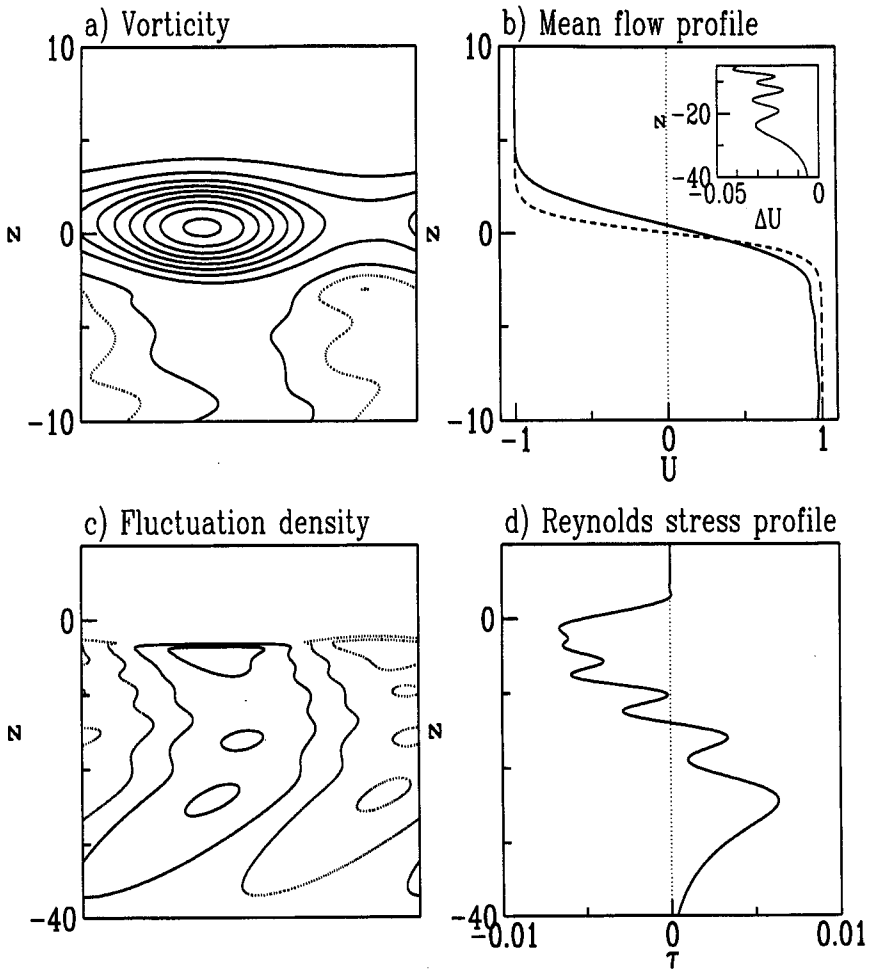

FIG. 8. Development of simulated hyperbolic tangent shear flow for JN^2 characterized by Eq. (2) with $J_0 = 0$, $J = 0.2$, $z_0 = 3$, and $R = 0.1$ at time $t = 100$. (a) Vorticity field shown by contours of 0.1; (b) horizontally averaged mean flow at $t = 100$ (solid curve) compared with mean flow at $t = 0$ (dashed curve), and inset diagram showing difference between these below $z = -5$; (c) fluctuation density field shown by contours of 0.3; and (d) Reynolds stress profile indicating weak downward transport of upstream momentum only near the leading edge of the IGW wavepacket.

vortex, some of this energy is converted to available potential form. During the first stages of these simulations they are dissimilar in that for large J the peak rate of transfer of kinetic energy between the waves and the mean flow is small and the baroclinic conversion of kinetic energy is large. Such behavior is anticipated since the development of the most unstable normal mode should become retarded when it grows to large amplitude in the presence of the more strongly stratified fluid in the far field. More kinetic energy is baroclinically converted to available potential energy when large amplitude IGW are generated. After time $t \approx 30$, the behavior of the three simulations diverges significantly. Figure 9a shows that kinetic energy is continuously extracted from the mean flow by eddies and that the kinetic energy of the eddies, in turn, is continuously converted into available potential energy form. This continuous conversion is not confined to the mixing region but is instead indicative of the extraction of energy from the mean flow by radiating waves. Likewise, as shown in Fig. 9b, mean flow kinetic energy is extracted by waves but the process is not so vigorous at late times. For the case in which $J = 0.2$ and only weak IGW radiation occurs, Fig. 9c shows that the direction of energy transfer is reversed after time $t \approx 50$ and that the mean flow kinetic energy slowly increases at the expense of stored available potential energy and eddy kinetic energy.

This figure gives some evidence of the way in which the nonlinear evolution of the most unstable mode develops so as to excite IGW. During the initial stages of the flow evolution the horizontal wavenumber of the disturbance remains unaltered and the horizontal phase speed changes to a small degree. These characteristics

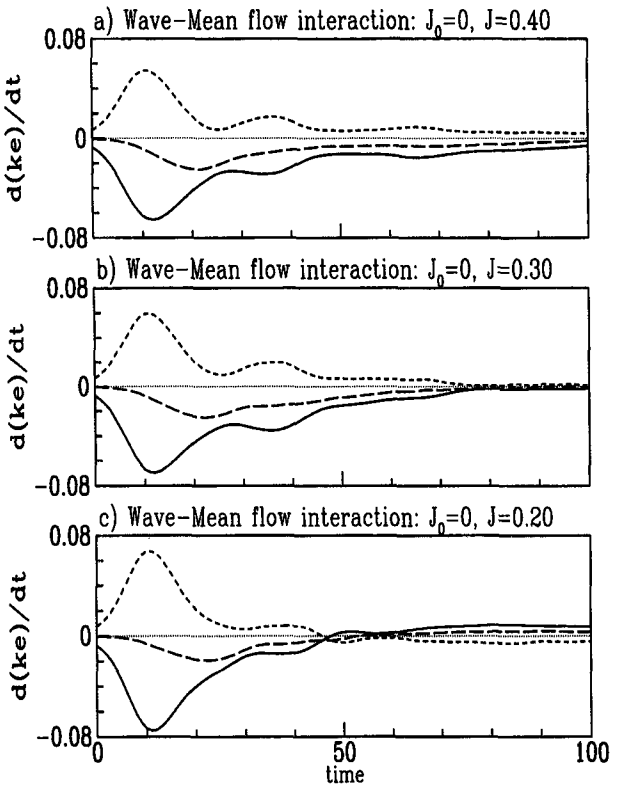

FIG. 9. A study of wave–mean flow interaction between times 0 and 100 for cases with the stratification characterized by $J_0 = 0$ and (a) $J = 0.4$, (b) $J = 0.3$, (c) $J = 0.2$. In each diagram the solid curve represents the change in mean flow kinetic energy due to nondiffusive effects, the short-dashed curve represents the nondiffusive change in the wave kinetic energy, and the long-dashed curve is the nondiffusive change of total kinetic energy due to the deposition of available potential energy. In the first two diagrams it is apparent that kinetic energy is continuously extracted from the mean flow by waves. The last diagram indicates that kinetic energy is returned to the mean flow by waves after time $t \approx 50$.

determine the frequency at which IGW are forced in the far field. After the mode saturates, in cases where the stratification in the far field is not sufficiently large to support radiating IGW, the eddy energy remains confined to the mixing region with no direct mechanism through which to excite waves. If the stratification is stronger in the far field, however, energy may be extracted from the mixing region by the direct excitation of IGW. This excitation stops when the mean flow is decelerated to such an extent that the frequency of forcing in the far field is larger than the buoyancy frequency or when the eddy energy of the mixing region is dissipated to such an extent that the amplitude of forcing is negligible. IGW are excited for a longer time if the stratification is larger because the far field can support a broader range of frequencies of IGW.

The energy transfer diagnostics illustrate the effects of the wave–mean flow interaction on IGW generation. In order to distinguish the effects of momentum redistribution due to viscous and eddy diffusion in the mixing region from the effects of momentum transport by waves, the Reynolds stress change is plotted between times $t = 0$ and 100 for the same three simulations as those discussed above regarding Fig. 9. In Fig. 10 the solid curve in each diagram shows the Reynolds stress τ_0 across $z = 0$, and the dashed curve is the Reynolds stress τ_{-5} across $z = z_\tau = -5$. The value $z_\tau = -5$ is chosen as a level close to the mixing region but sufficiently far below it so that motion across z_τ is wavelike. Here τ_0 gives a measure of the transport of momentum by eddies and waves downward across the inflection point of the shear in the mixing region; τ_{-5} gives a measure of the momentum transport away from the mixing region by waves alone.

In all three cases, during the development of the most unstable mode, horizontal momentum is transported vertically across $z = 0$, this flux being largest about

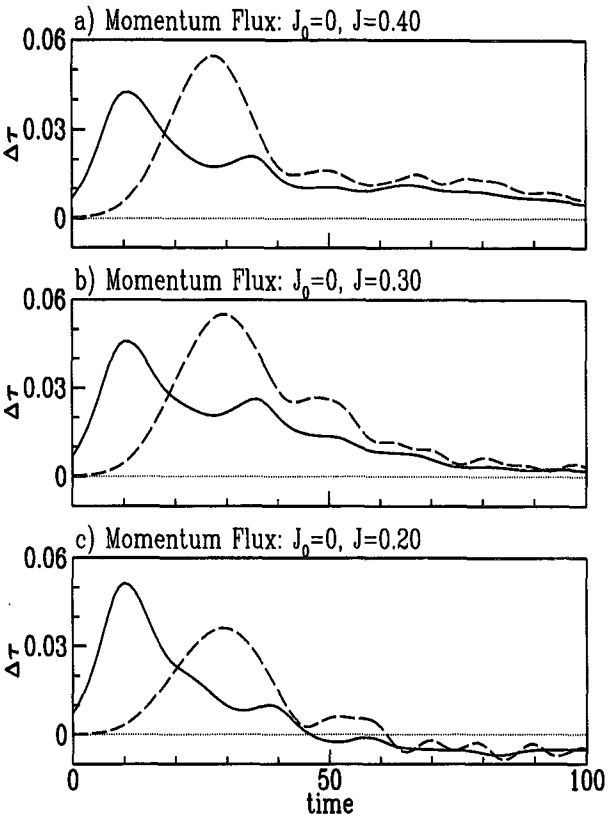

FIG. 10. A comparison of the vertical transport of horizontal momentum by IGW with the redistribution of horizontal momentum in the mixing region by eddies between times 0 and 100 for cases with the stratification characterized by $J_0 = 0$ and (a) $J = 0.4$, (b) $J = 0.3$, (c) $J = 0.2$. In each diagram the solid curve represents the Reynolds stress at $z = 0$ and the dashed curve represents the Reynolds stress at $z = -5$. The latter is a measure of the transport of horizontal momentum away from the mixing region by IGW. Only in (a) and (b) is it apparent that IGW extract horizontal momentum away from the mean flow for long times.

time $t \approx 11$. In Figs. 10a and 10b for which $J = 0.4$ and 0.3, respectively, the momentum flux below $z = z_\tau$ becomes large after $t \approx 20$. The peak Reynolds stress is $\tau_{-5} \approx 0.055$ (≈ 8.8 N m^{-2} in dimensional units; see Table 1). At all times in these two simulations, the flux of upstream momentum is directed downward, although this flux is greater in the simulation with $J = 0.4$. Figure 10c shows the Reynolds stress for the simulation with $J = 0.2$. Here its peak value across z_τ is $\tau_{-5} \approx 0.035$ (≈ 5.6 N m^{-2}) and after $t \approx 60$ the upstream momentum flux is redirected upward.

A measure of the drag to the mixing region due to IGW emission is calculated in terms of the average deceleration $\bar{D}$ between $z = -5$ and $z = 5$ over the duration of each simulation. In Table 1, $\bar{D}$ is given in dimensional units using $\mathcal{U} = 0.4$ m s^{-1} and $\mathcal{L} = 10$ m, emphasizing the substantial drag exerted on the mean flow due to the generation of IGW. For example, when large amplitude IGW radiate (the case with $J_0 = 0$, $J = 0.4$), the flow in the mixing region decelerates on average by 2.9×10^{-5} m s^{-2}; in other words, the flow speed decreases on average by approximately 5 m s^{-1} in less than one hour due to IGW emission. Because the simulations are restricted to two dimensions, this is probably an overestimate of the degree of drag that occurs in fully three dimensional turbulent flow. Nonetheless, it demonstrates the potentially nonnegligible effect that the generation of IGW by shear instability may have upon the mean flow of the equatorial undercurrent.

If the momentum is redistributed locally across $z = 0$ due to eddy mixing alone, then $\tau_{-5} = 0$. Hence a convenient measure of the relative importance of momentum transport by IGW compared with the local momentum redistribution by eddy mixing and IGW at time t is given by

$$M_t = \left(\int_0^t \tau_{-5} dt\right) \Big/ \left(\int_0^t \tau_0 dt\right). \qquad (23)$$

If at late times $M_t \approx 0$, then the momentum is locally redistributed due to eddy mixing. If $M_t \approx 1$, the momentum is efficiently transported away from the mixing region by waves. Table 3 lists values of M_{100} for a range of simulations in which the mixing region is both stratified and unstratified. The numbers in bold represent values for which the penetration condition is satisfied and underlined numbers represent values for which the phase speed condition is satisfied. The values for the stratified mixing region cases will be discussed in the section 3b. If the mixing region is unstratified, the penetration condition is satisfied if $J > 0.37$, and the phase speed condition is satisfied if $J > 0.24$. Table 3 shows that $M_{100} \approx 1.16 \pm 0.01$ for J between 0.25 and 0.45, and M_{100} is significantly smaller for $J = 0.20$ and 0.15. Therefore, for these simulations the phase speed condition effectively predicts the circumstances under which IGW may efficiently extract energy and momentum from an unstable shear flow. The penetration condition is sufficient but not necessary for these cases.

TABLE 3. Values of M_t defined by Eq. (23) at time $t = 100$ calculated for a range of simulations with basic states given by Eq. (2) with $z_0 = 3$, $R = 0.1$. M_t is a measure of the efficiency by which IGW transport momentum away from the mixing region. If M_t is small, the momentum is redistributed about the shear by eddy mixing. If $M_t \approx 1$, IGW transport substantial momentum away from the mixing region. Bold numbers represent values for which the penetration condition is satisfied; underlined numbers represent values for which the phase speed condition is satisfied.

	$J = 0.45$	0.40	0.35	0.30	0.25	0.20	0.15
$J_0 = 0.0$	**1.16**	**1.17**	1.15	1.17	1.16	0.89	0.48
$J_0 = 0.05$	**1.03**	**1.00**	**0.95**	0.97	0.10	0.08	

b. Simulations with a stratified mixing region

In cases where the stratification is nonnegligible in the mixing region, the flow evolution is markedly different with regard to both the generation of IGW by the most unstable mode and the long time evolution of the simulations. Two simulations are examined in detail that illustrate the range of behaviors. In both, $z_0 = -3$, $R = 0.1$, and $J_0 = 0.05$ so that the minimum gradient Richardson number is well below the Miles–Howard 1/4 limit, and the growth rate of the most unstable mode is comparable to that in cases with $J_0 = 0$. In the first simulation, to be discussed below, the far-field stratification is $J = 0.4$, which is sufficiently large that the most unstable mode is capable of directly exciting IGW. In the second simulation $J = 0.2$, and IGW are not directly excited.

The characteristics of the most unstable mode for the basic state given by Eq. (2) with $z_0 = 3$, $R = 0.1$, $J_0 = 0.05$, and $J = 0.4$ are given in Table 2, which shows that both the phase speed and penetration conditions are satisfied. Large amplitude IGW are therefore anticipated in this case. Figure 11 shows the vorticity field at time $t = 100$ of the simulation with $J = 0.4$ over a vertical range between $z = -10$ and 10. The contours are shown by intervals of 0.3, positive (negative) contours shown by solid (dashed) curves. Unlike the vorticity field shown in Fig. 7a, this diagram shows significant mixing associated with the vortex that develops from the most unstable mode. Although the resolution of this simulation is not adequate to accurately represent mixing at very small scales, simulations at higher resolution (not shown here) reveal that the large-scale structures and, in particular, the radiating wave field, are sufficiently well represented here. Regions of strong negative vorticity are apparent near the braids on either side of the vortex core. In their study of uniformly stratified jet flow, Sutherland and Peltier (1994) observed similar patches of negative vorticity and showed that they were generated by baroclinic torques that develop where heavy fluid is carried downward

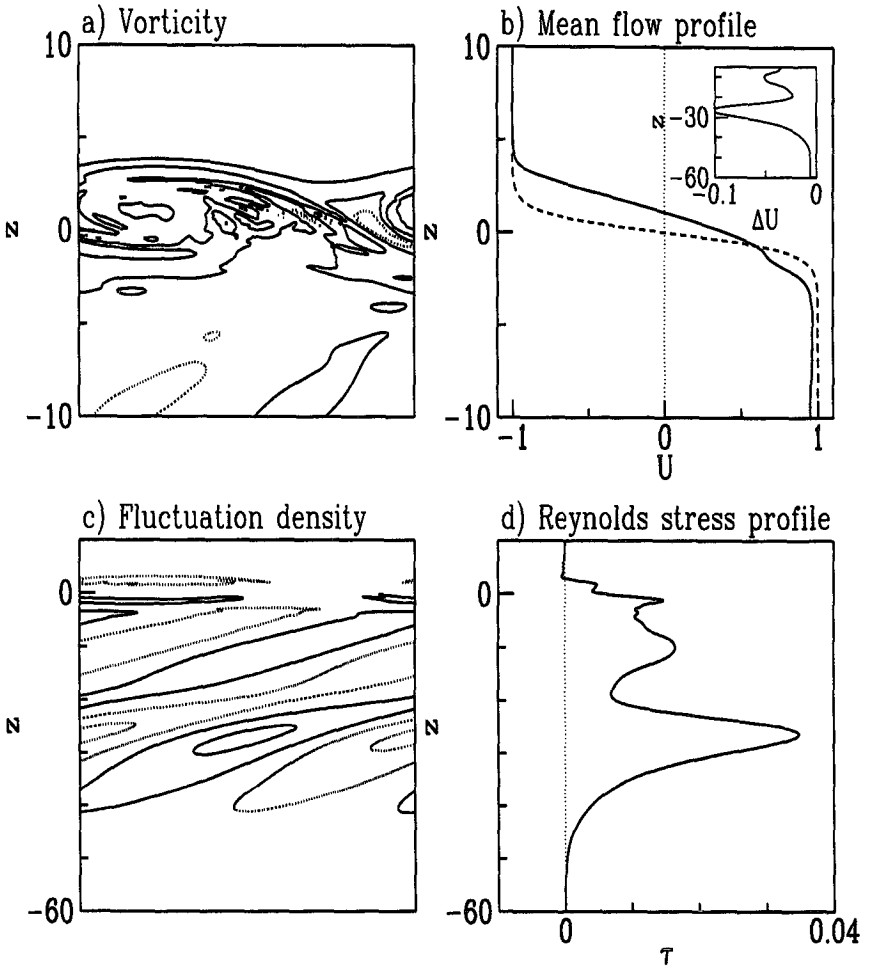

FIG. 11. Development of simulated hyperbolic tangent shear flow for JN^2 characterized by Eq. (2) with $J_0 = 0.05$, $J = 0.4$, $z_0 = 3$, and $R = 0.1$ at time $t = 100$. (a) Vorticity field shown by contours of 0.3; (b) horizontally averaged mean flow at $t = 100$ (solid curve) compared with mean flow at $t = 0$ (dashed curve), and inset diagram showing difference between these below $z = -5$; (c) fluctuation density field shown by contours of 0.4; and (d) Reynolds stress profile indicating downward transport of upstream momentum.

and light fluid is carried upward by the flanking large-scale vortical motion.

Despite the different structure of the mixing region between cases with $J_0 = 0$ and $J_0 = 0.05$, the acceleration of the mean flow above $z = 0$ due to the downward transport of momentum by IGW and the characteristics of the waves themselves are similar in the two cases. Figure 11b compares the horizontally averaged mean flow at time $t = 100$ (solid line) with the initial mean flow (dashed curve) over the same vertical range as that in which the vorticity field is shown and demonstrates the significant drag on the mean flow induced by the radiation of IGW. The momentum deficit in the mixing region is accounted for by the momentum transported to great depths by IGW as shown in the inset. In particular, the mean flow at $t = 100$ is decelerated from 1.0 to below 0.9 at depths around $z = -26$. In Fig. 11c contours of the fluctuation density field are shown by intervals of 0.4 with positive (negative) contours given by solid (dashed) curves. The field is shown over the full vertical range of the simulation from $z = -60$ to 10. The amplitude of the IGW is comparable to that in the unstratified mixing region case with $J_0 = 0$ and $J = 0.4$, although the waves in this case have not propagated downward as far by time $t = 100$. This is primarily because the vertical wavenumber of the IGW in this case is smaller and the vertical group velocity is reduced. Nonetheless, the Reynolds stress profile shown in Fig. 11d over $z = -60$ to 10 is positive below $z = 0$ and the peak Reynolds stress is comparable to that in the unstratified case.

For the stratified mixing region case with $J_0 = 0.05$ and $J = 0.2$, the characteristics of the most unstable mode given in Table 2 show that neither the phase speed nor the penetration condition are satisfied and so large amplitude IGW are not expected to occur. The vorticity field at time $t = 100$ of the simulation for this case is shown by contours of interval 0.3, in Fig. 12a, illustrating small-scale mixing where the shear is large. The momentum associated with the shear is redistributed about $z = 0$ and no significant IGW radiation occurs. The local redistribution of momentum is explicitly demonstrated in Fig. 12b, which compares the mean flow at $t = 100$ (solid curve) with that at $t = 0$ (dashed curve). No significant deceleration of the flow occurs below $z = -10$. The fluctuation density is large only near the mixing region and this field is shown for $-10 \leq z \leq 10$ by contours of interval 0.4 in Fig. 12c. The Reynolds stress profile is shown over the same vertical range in Fig. 12d. The peak is largest at $z = 0$ and the Reynolds stress is negligible below $z = -10$.

As in Fig. 9, the wave–mean flow interaction in the stratified mixing region cases between times $t = 0$ and 100 is illustrated in Fig. 13, which shows the time rate of change of nondiffusive mean flow kinetic energy (solid curve), of nondiffusive eddy kinetic energy (short-dashed curve), and of the baroclinic conversion of eddy kinetic energy to available potential energy (long-dashed curve). These are shown for cases with $J_0 = 0.05$ and (a) $J = 0.4$, (b) $J = 0.3$, and (c) $J = 0.2$. Although in the stratified mixing region cases the peak rate of change of mean flow kinetic energy is smaller compared with the counterpart examples in the unstratified mixing region cases (i.e., Fig. 9), the interaction between the waves and the mean flow is sig-

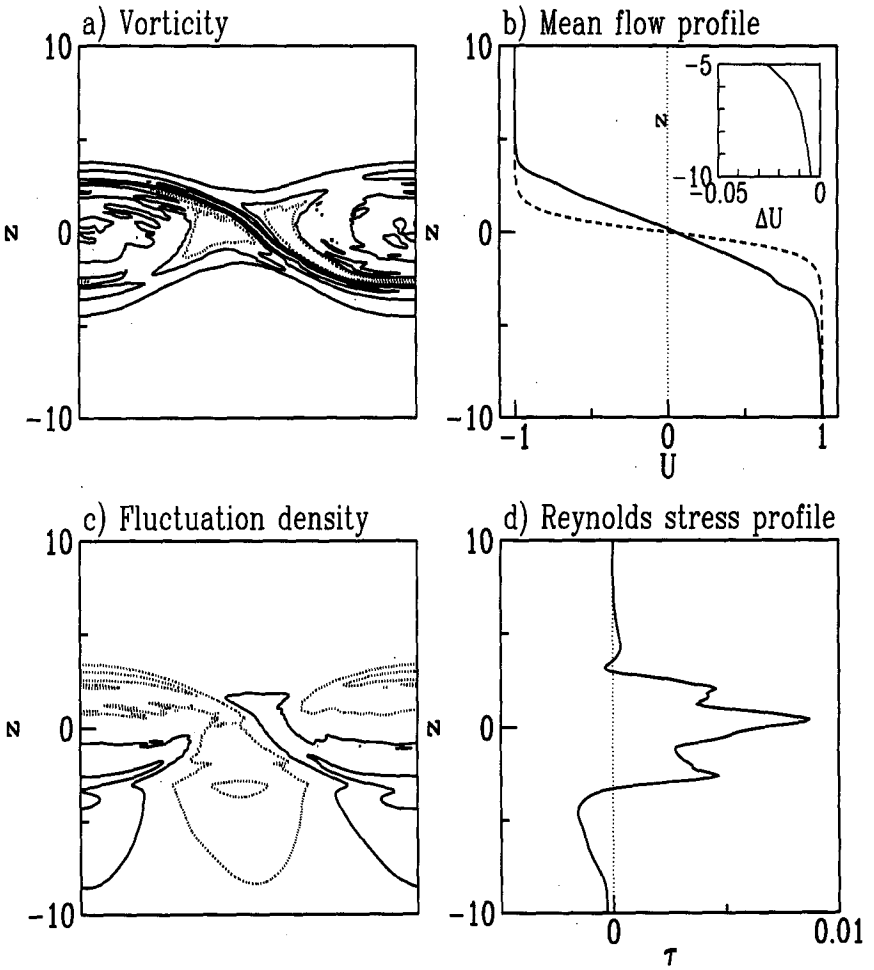

FIG. 12. Development of simulated hyperbolic tangent shear flow for JN^2 characterized by Eq. (2) with $J_0 = 0.05$, $J = 0.2$, $z_0 = 3$, and $R = 0.1$ at time $t = 100$. (a) Vorticity field shown by contours of 0.3; (b) horizontally averaged mean flow at $t = 100$ (solid curve) compared with mean flow at $t = 0$ (dashed curve), and inset diagram showing difference between these below $z = -5$; (c) fluctuation density field shown by contours of 0.4; and (d) Reynolds stress profile indicating downward transport of upstream momentum.

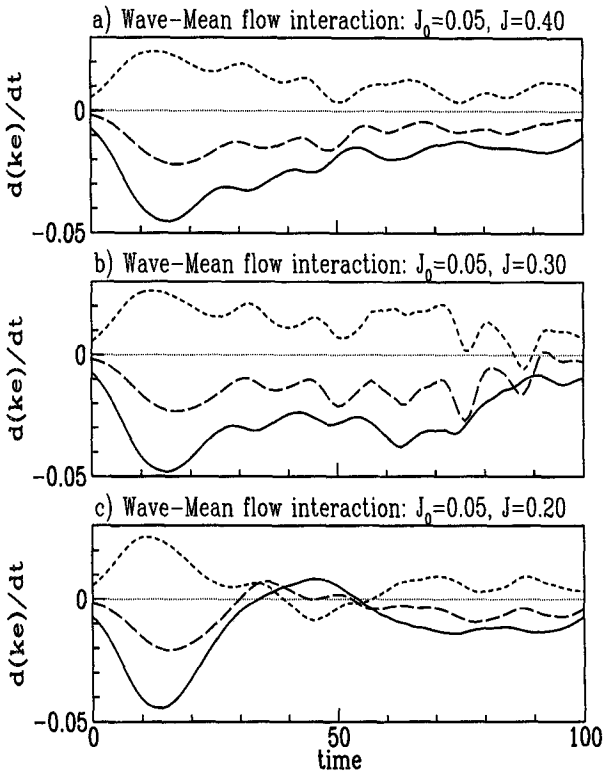

FIG. 13. A study of wave–mean flow interaction between times 0 and 100 for cases with the stratification characterized by $J_0 = 0.05$ and (a) $J = 0.4$, (b) $J = 0.3$, (c) $J = 0.2$. In each diagram the solid curve represents the change in mean flow kinetic energy due to nondiffusive effects, the short-dashed curve represents the nondiffusive change in the wave kinetic energy, and the long-dashed curve is the nondiffusive change of total kinetic energy due to the deposition of available potential energy. In the first two diagrams it is apparent that kinetic energy is continuously extracted from the mean flow by waves and this process continues efficiently for long times compared with the case for $J_0 = 0$ (see Fig. 9). The last diagram indicates that kinetic energy is returned to the mean flow by waves after time $t \approx 40$.

nificant for longer times. The effect of the stratification in the mixing region is to enhance the interactions between the waves and the mean flow by allowing the transfer of eddy energy between available potential and kinetic energy forms where the mixing is most intense. In all three cases, the baroclinic conversion of eddy kinetic energy to available potential energy is significant during the early development of the initial disturbance and energy continues to be converted in this sense at late times both due to IGW generation and mixing in the shear. The conversion is much larger for the cases with $J = 0.4$ and $J = 0.3$ in which large amplitude IGW are generated.

Figure 14 shows the effect of the wave–mean flow interaction upon the flux of momentum across $z = 0$, and $z = z_T = -5$ between times $t = 0$ and 100. In (a) and (b) for which $J = 0.4$ and 0.3, respectively, and IGW are directly excited by the development of the most unstable mode, qualitatively similar behavior occurs between the stratified and unstratified mixing region cases (i.e., Figs. 10a and 10b) in that IGW continually extract momentum from the mixing region throughout the duration of the simulations. In the stratified mixing region case, although the peak Reynolds stress across $z = 0$ is smaller (≈ 0.03 for $J = 0.4$ and ≈ 0.04 for $J = 0.3$; see also Table 1), the momentum flux is large for longer times. In (c), for which $J = 0.2$ and IGW are not directly excited by the most unstable mode, negligible momentum is transported away from the mixing region.

The average deceleration of the mixing region due to IGW emission in the case with $J_0 = 0.05$ and $J = 0.4$ is comparable to that when $J_0 = 0$ (see Table 1). When $J = 0.2$, however, the drag is negligible.

The efficiency M_t by which the radiation of IGW influences the redistribution of momentum in the mixing region at time t as characterized by Eq. (23) is listed, for $t = 100$, in Table 3 for a range of simulations

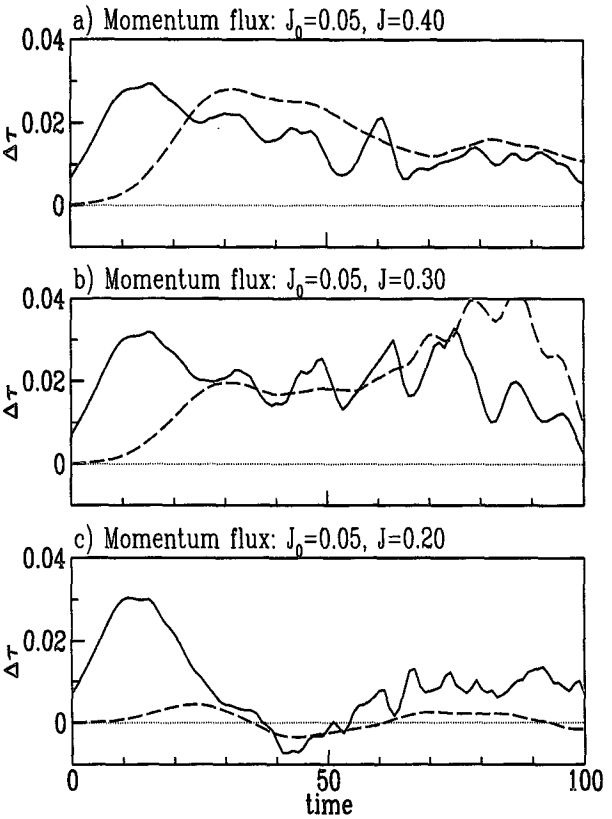

FIG. 14. A comparison of the vertical transport of horizontal momentum by IGW with the redistribution of horizontal momentum in the mixing region by eddies between times 0 and 100 for cases with the stratification characterized by $J_0 = 0.05$ and (a) $J = 0.4$, (b) $J = 0.3$, (c) $J = 0.2$. In each diagram the solid curve represents the Reynolds stress at $z = 0$ and the dashed curve represents the Reynolds stress at $z = -5$. Only in (a) and (b) is it apparent that IGW extract horizontal momentum away from the mean flow for long times and this process continues to be efficient over longer times than in the case with $J_0 = 0$ (see Fig. 10).

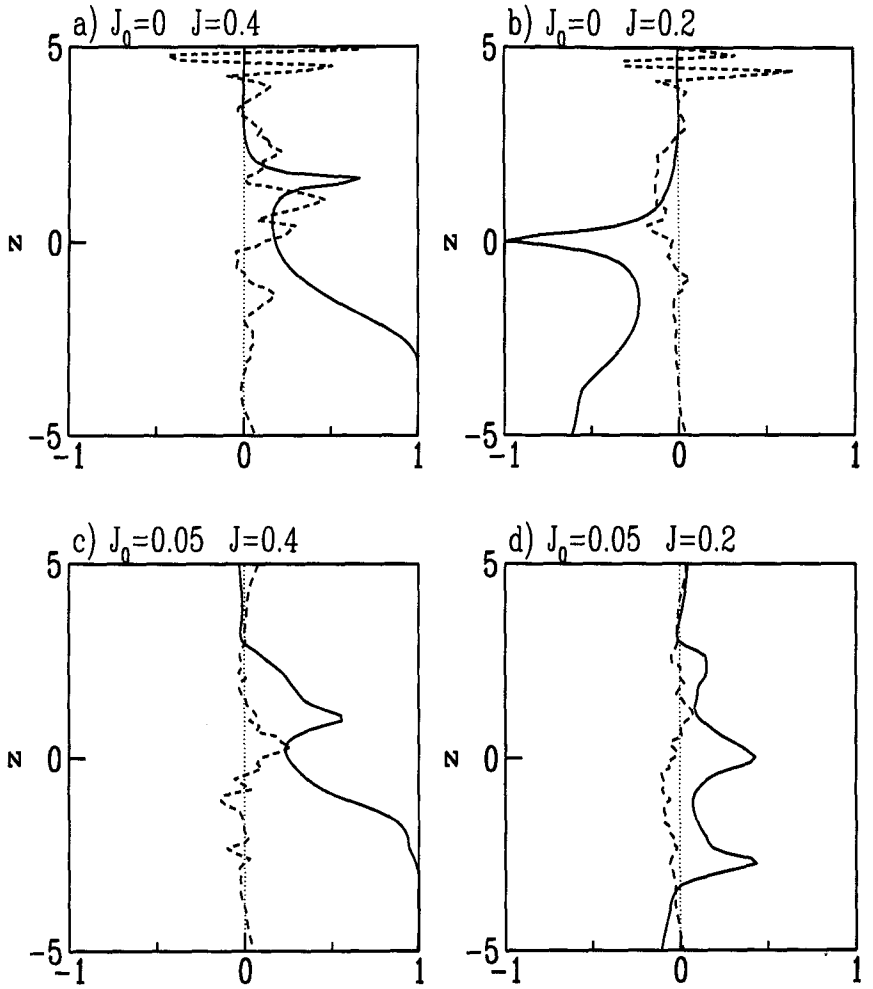

FIG. 15. Profiles of the linear correlation coefficients of horizontal and vertical velocity corr(u', w') (solid line) and of vertical velocity and fluctuation density corr(w', ρ') (dashed line) calculated at time $t = 100$ for cases with the stratification characterized by (a) $J_0 = 0$, $J = 0.4$, (b) $J_0 = 0$, $J = 0.2$, (c) $J_0 = 0.05$, $J = 0.4$, and (d) $J_0 = 0.05$, $J = 0.2$.

with varying far-field values of stratification J. As with the unstratified case, numbers in bold represent values for which the penetration condition is satisfied (which for $J_0 = 0.05$ occurs if $J > 0.32$) and underlined numbers represent values for which the phase speed condition is satisfied (which for $J_0 = 0.05$ occurs if $J > 0.24$). For cases in which $J_0 = 0.05$, $M_{100} \approx 0.99 \pm 0.04$ when the far-field stratification $J \geq 0.30$. This value is moderately less than the efficiency calculated for the unstratified mixing region when the phase speed condition is satisfied, as might be expected since there is more small-scale turbulence in this case. Even though the phase speed condition is satisfied for $J = 0.25$, the emission of IGW in this case is weak. Compared with its results for the unstratified mixing region case, the phase speed condition is not as successful predicting whether large amplitude IGW generation will occur.

In summary, if the mixing region is unstratified, large amplitude IGW are excited by the growth of the most unstable mode of the shear if the thermocline is strongly stratified. A compact IGW wavepacket of smaller amplitude is generated by a nonlinear mechanism if the thermocline is more weakly stratified. If the mixing region is stratified, the excitation of IGW by the growth of the most unstable mode is more efficient when the thermocline is stratified, and IGW excitation is strongly inhibited when the thermocline is more weakly stratified.

The coupling between radiating IGW and the mixing region at time 100 in four cases is demonstrated in Fig. 15, which shows profiles of the linear correlation coefficients corr(u', w') and corr(w', ρ') at depths between $z = -5$ and 5. The four cases are the same as those considered in Fig. 5 for which the correlation profiles were deduced from the most unstable modes

of linear theory: in (a) $J_0 = 0$, $J = 0.4$, in (b) $J_0 = 0$, $J = 0.2$, in (c) $J_0 = 0.05$, $J = 0.4$, and in (d) $J_0 = 0.05$, $J = 0.2$. When the thermocline is strongly stratified propagating IGW occur below $z \approx -2.5$, where $\mathrm{corr}(u', w') > 0.95$ and $\mathrm{corr}(w', \rho') \approx 0$. When the thermocline is moderately stratified, $\mathrm{corr}(u', w')$ is close to zero (Fig. 15d) or even negative (Fig. 15b). In the latter case IGW propagate upward toward the mixing region at $t = 100$.

Large amplitude IGW develop in an unstable shear flow if they are excited directly by the most unstable normal mode of linear theory. As a crude estimate, in practice, this occurs if the ratio of N_*^2 in the mixing region to the maximum squared shear strength $S_*^2 = \max(|dU/dz|^2)$ is less than ≈ 0.25 and the ratio of N_*^2 in the thermocline to S_*^2 exceeds ≈ 0.25, provided the thermocline is situated sufficiently far below the shear unstable region. For example, regarding the basic state shown in Fig. 2, which is derived from observations, $S_*^2 \approx 0.0012\ \mathrm{s}^{-2}$ and $N_*^2 < 0.0003\ \mathrm{s}^{-2}$ down to 70-m depth. Near the thermocline $N_*^2 \approx S_*^2$. Therefore, strong IGW generation from shear flow instability is not unlikely.

4. Discussion and conclusions

The generation of IGW by shear instability is proposed as a mechanism by which momentum is transported downward from the upper flank of the equatorial undercurrent, thus acting simultaneously as a momentum sink to the undercurrent and, potentially, as a momentum source to the deep equatorial countercurrents. Linear theory and nonlinear numerical simulations demonstrate that IGW are generated under a robust range of initial conditions but occur on such small horizontal length scales (of the order of the shear depth ~ 10 m) and fast timescales (of the order of minutes) that direct observation of them is challenging. Some support appears to be provided, however, by Hebert et al. (1992) who observed an IGW wavepacket associated with an overturning event on the upper flank of the Pacific equatorial undercurrent.

In this paper, many of the diagnostics that have been employed may be used to ascertain whether the generation of IGW by shear instability has actually occurred. On the basis of linear theory, conditions have been determined under which a shear unstable basic state is capable of exciting large amplitude IGW ("large" in the sense that the emission of IGW nonnegligibly influences the nonlinear development of the mixing region). Qualitatively, large amplitude IGW are generated if a shear flow is unstable in weakly stratified fluid and the surrounding fluid is strongly stratified. Quantitatively, this is assessed by examining the characteristics of the most unstable mode of linear theory and testing whether these satisfy the phase speed condition, Eq. (8), and the penetration condition, Eq. (9). Nonlinear numerical simulations support the linear theory assumption that the phase speed condition is necessary and the penetration condition is sufficient for strong IGW generation. The phase speed condition more accurately poses a necessary and sufficient condition if the mixing region is weakly stratified.

Transport of momentum and mass have been studied by calculating the linear correlation coefficients $\mathrm{corr}(u', w')$ and $\mathrm{corr}(w', \rho')$. Where waves propagate well below the mixing region, the former correlation is close to 1 and the latter is close to 0, as expected for plane IGW. This analysis clearly distinguishes the mixing region from the far-field region where IGW propagate unaffected by mixing. Although the simultaneous measurement in the open ocean of vertical velocity, density, and horizontal velocity is challenging, it would provide information that could indicate whether surface and deep ocean mixing are linked by IGW generation, propagation, and breaking. The technology for such measurements now appears to be accessible as Fleury and Lueck (1994) have shown by making direct estimates of the vertical heat flux.

Though it is beyond the scope of this work to examine what processes would cause the flow itself to become unstable, one might speculate, in light of the ambient conditions preceding the observation by Hebert et al. (1992), that cooling and convective mixing near the surface in the presence of the underlying marginally stable shear flow may be sufficient to reduce the stratification above the thermocline and destabilize the upper flank of the equatorial undercurrent. A detailed study of convective processes in the presence of shear is required to examine this hypothesis. The upward displacement of the thermocline due to the "shear wave" may also be an essential ingredient because this may act to facilitate the coupling between shear instability in the mixing region and radiating IGW in the thermocline.

Finally, it is speculated upon but not examined here that IGW once generated by shear are capable of propagating to great depths (below 300 m) where they act as a source of momentum driving the zonal countercurrents. The basic states studied here fix U and N^2 constant at great depths in order to easily examine the characteristics of downward propagating IGW. In reality, both U and N^2 decrease below the undercurrent core, but if the basic state is dynamically stable over many shear depths below the mixing region, as in the case of the observations motivating this work, it is assumed that variations of U and N^2 at great depths should not significantly affect the behavior of the dynamically unstable flow within the mixing region during the early stages of the flow development. Although such variations of the basic state should not, therefore, affect IGW generation from the upper flank of the undercurrent, they would greatly affect IGW propagation. For small amplitude wavepackets, ray theory [e.g., see Lighthill (1978) §4.6] predicts that if N^2 decreases sufficiently, IGW reflect from a depth (the "evanescent

level") where the intrinsic wave frequency equals N, and if U decreases sufficiently, IGW asymptotically approach a depth (the "critical level") where the horizontal phase speed of the waves equals the speed of the background flow. In the latter case IGW ultimately break and the associated momentum flux convergence acts to accelerate the mean flow near the critical level. Indirect evidence for the near-surface generation and deep ocean breaking of IGW may possibly be inferred from one of the observations by Peters et al. (1995) who, four days preceding the observations by Hebert et al. (1992), recorded velocity and N^2 profiles at 0°, 140°W that showed strong mixing near 200-m depth (see Fig. 15 of their paper). Near the surface occurred strong mixing associated with the diurnal cycle and the presence of a "shear wave" (Peters et al. 1991). Under suitable conditions it may be that the two mixing events were linked: IGW generated near the surface extracted momentum from the mixing region and transported it downward to 200-m depth where the waves encountered a critical level and deposited momentum to the mean flow.

Both the reduced stratification and alternating currents below the thermocline would seem to limit the depth to which IGW may propagate. However, it seems now that large amplitude IGW may propagate to depths greater than those predicted by ray theory. Specifically, Sutherland (1996) examined the nonlinear evolution of a large amplitude IGW wavepacket in nonuniformly stratified fluid and showed that, due in part to transient forcing but also significantly due to nonlinear processes, large amplitude IGW may propagate into regions in which the initial wavepacket is evanescent. The effects of variations in the background flow upon the propagation of large amplitude IGW is currently under investigation.

Acknowledgments. I would like to thank Bill Smyth who first directed my attention to the interesting problems involved in understanding the dynamics of the equatorial undercurrent. I am also grateful to Paul Linden and the two anonymous reviewers of this paper for their useful comments. This work has been supported in part by the Natural Environment Research Council Grant GR3/09399.

REFERENCES

Bretherton, F. P., 1969: Momentum transport by gravity waves. *Quart. J. Roy. Meteor. Soc.*, **95,** 213–243.

Chimonas, G., and J. R. Grant, 1984a: Shear excitation of gravity waves. Part I: Modes of a two-scale atmosphere. *J. Atmos. Sci.*, **41,** 2269–2277.

——, and ——, 1984b: Shear excitation of gravity waves. Part II: Upscale scattering from Kelvin–Helmholtz waves. *J. Atmos. Sci.*, **41,** 2278–2288.

Clark, A. J., 1983: The reflection of equatorial waves from oceanic boundaries. *J. Phys. Oceanogr.*, **13,** 1193–1207.

Davis, P. A., and W. R. Peltier, 1976: Resonant parallel shear instability in the stably stratified planetary boundary layer. *J. Atmos. Sci.*, **33,** 1287–1300.

——, and ——, 1979: Some characteristics of the Kelvin–Helmholtz and resonant overreflection modes of shear flow instability and of their interaction through vortex pairing. *J. Atmos. Sci.*, **36,** 2394–2412.

Dillon, T. M., J. N. Moum, T. K. Chereskin, and D. R. Caldwell, 1989: Zonal momentum balance at the equator. *J. Phys. Oceanogr.*, **19,** 561–570.

Drazin, P. G., and L. N. Howard, 1966: Hydrodynamic stability of parallel flow of inviscid fluid. *Adv. Appl. Math.*, **9,** 1–89.

Eriksen, C., 1982: Geostrophic equatorial deep jets. *J. Mar. Res.*, **40,** 143–157.

——, 1985: Moored observations of deep low-frequency motions in the central Pacific Ocean: Vertical structure and interpretation as equatorial waves. *J. Phys. Oceanogr.*, **15,** 1085–1113.

Firing, E., 1987: Deep zonal currents in the central equatorial Pacific. *J. Mar. Res.*, **45,** 791–812.

Fleury, M., and R. G. Lueck, 1994: Direct heat flux estimates using a towed vehicle. *J. Phys. Oceanogr.*, **24,** 801–818.

Fritts, D. C., 1982: Shear excitation of atmospheric gravity waves. *J. Atmos. Sci.*, **39,** 1936–1952.

——, and G. D. Nastrom, 1992: Sources of mesoscale variability of gravity waves. Part II: Frontal, convective, and jet stream excitation. *J. Atmos. Sci.*, **49,** 111–127.

Harvey, R. R., and W. C. Patzert, 1976: Deep current measurements suggest long waves in the eastern equatorial Pacific. *Science,* **193,** 883–885.

Hazel, P., 1972: Numerical studies of the stability of inviscid stratified shear flows. *J. Fluid Mech.*, **51,** 39–61.

Hebert, D., J. N. Moum, C. A. Paulson, D. R. Caldwell, T. K. Chereskin, and M. J. McPhaden, 1991: The role of the turbulent stress divergence in the equatorial Pacific zonal momentum balance. *J. Geophys. Res.*, **96**(C4), 7127–7136.

——, ——, ——, and ——, 1992: Turbulence and internal waves at the equator. Part II: Details of a single event. *J. Phys. Oceanogr.*, **22,** 1346–1356.

Howard, L. N., 1961: Note on a paper by John W. Miles. *J. Fluid Mech.*, **10,** 509–512.

Klaassen, G. P., and W. R. Peltier, 1985: The onset of turbulence in finite-amplitude Kelvin–Helmholtz billows. *J. Fluid Mech.*, **155,** 1–35.

Lalas, D. P., and F. Einaudi, 1976: On the characteristics of gravity waves generated by atmospheric shear layers. *J. Atmos. Sci.*, **33,** 1248–1259.

Lighthill, M. J., 1978: *Waves in Fluids.* Cambridge University Press, 504 pp.

Lindzen, R. S., 1974: Stability of a Helmholtz velocity profile in a continuously stratified infinite Boussinesq fluid—Applications to clear air turbulence. *J. Atmos. Sci.*, **31,** 1507–1514.

——, and A. J. Rosenthal, 1976: On the instability of Helmholtz velocity profiles in stably stratified fluids when a lower boundary is present. *J. Geophys. Res.*, **81,** 1561–1571.

Longsdale, P., 1977: Inflow of bottom water to the Panama basin. *Deep-Sea Res.*, **24,** 1065–1101.

Lott, F., H. Kelder, and H. Teitelbaum, 1992: A transition from Kelvin–Helmholtz instabilities to propagating wave instabilities. *Phys. Fluids A,* **4,** 1990–1997.

Luyten, J., and J. Swallow, 1976: Equatorial undercurrents. *Deep-Sea Res.*, **23,** 499–524.

McIntyre, M. E., and M. A. Weissman, 1978: On radiating instabilities and resonant overreflection. *J. Atmos. Sci.*, **35,** 1190–1196.

Miles, J. W., 1961: On the stability of heterogeneous shear flows. *J. Fluid Mech.*, **10,** 496–508.

Muench, J., E. Kunze, and E. Firing, 1994: The potential vorticity structure of equatorial deep jets. *J. Phys. Oceanogr.*, **24,** 418–428.

Pedlosky, J., 1987: *Geophysical Fluid Dynamics.* 2d ed. Springer Verlag, 710 pp.

Peters, H., M. C. Gregg, and T. B. Sanford, 1991: Equatorial and off-equatorial fine-scale and large-scale shear variability at 140°W. *J. Geophys. Res.*, **96,** 16 913–16 928.

——, ——, and ——, 1995: Detail and scaling of turbulent overturns in the Pacific Equatorial Undercurrent. *J. Geophys. Res.*, **100,** 18 349–18 368.

Skyllingstad, E. D., and D. W. Denbo, 1994: The role of internal gravity waves in the equatorial current system. *J. Phys. Oceanogr.*, **24,** 2093–2110.

Smyth, W., and W. Peltier, 1989: The transition between Kelvin–Helmholtz and Holmboe instability: An investigation of the overreflection hypothesis. *J. Atmos. Sci.*, **46,** 3698–3720.

——, and ——, 1992: Spectral transfers in 2D anisotropic flow. *Phys. Fluids A,* **4,** 340–349.

Sutherland, B. R., 1996: Internal gravity wave radiation into weakly stratified fluid. *Phys. Fluids,* **8,** 430–441.

——, and W. R. Peltier, 1992: The stability of stratified jets. *Geophys. Astrophys. Fluid Dyn.*, **66,** 101–131.

——, and ——, 1994: Turbulence transition and internal wave generation in density stratified jets. *Phys. Fluids A,* **6,** 1267–1284.

——, and ——, 1995: Internal gravity wave emission into the middle atmosphere from a model tropospheric jet. *J. Atmos. Sci.*, **52,** 3214–3235.

——, C. P. Caulfield, and W. R. Peltier, 1994: Internal wave generation and hydrodynamic instability. *J. Atmos. Sci.*, **51,** 3261–3280.

Wijesekera, H. W., and T. M. Dillon, 1991: Internal waves and mixing in the upper equatorial Pacific ocean. *J. Geophys. Res.*, **96,** 7115–7126.

Zabusky, N. J., and G. S. Deem, 1971: Dynamical evolution of two-dimensional unstable shear flows. *J. Fluid Mech.*, **47,** 353–379.